



# Stellar Properties for a Comprehensive Collection of Star-forming Regions in the SDSS APOGEE-2 Survey\*

Carlos G. Román-Zúñiga<sup>1</sup> , Marina Kounkel<sup>2,3</sup> , Jesús Hernández<sup>1</sup> , Karla Peña Ramírez<sup>4</sup> , Ricardo López-Valdivia<sup>1</sup> , Kevin R. Covey<sup>3</sup> , Amelia M. Stutz<sup>5,6</sup> , Alexandre Roman-Lopes<sup>7</sup> , Hunter Campbell<sup>3</sup> , Elliott Khilfeh<sup>3</sup> , Mauricio Tapia<sup>1</sup> , Guy S. Stringfellow<sup>8</sup> , Juan José Downes<sup>9</sup> , Keivan G. Stassun<sup>2</sup> , Dante Minniti<sup>10,11</sup> , Amelia Bayo<sup>12,13</sup> , Jinyoung Serena Kim<sup>14</sup> , Genaro Suárez<sup>15,16</sup> , Jason E. Ybarra<sup>17</sup> , José G. Fernández-Trincado<sup>18</sup> , Penélope Longa-Peña<sup>4</sup> , Valeria Ramírez-Preciado<sup>1</sup> , Javier Serna<sup>1</sup> , Richard R. Lane<sup>19</sup> , D. A. García-Hernández<sup>20</sup> , Rachael L. Beaton<sup>21,22</sup> , Dmitry Bizyaev<sup>23,24</sup> , and Kaike Pan<sup>23</sup>

<sup>1</sup> Universidad Nacional Autónoma de México, Instituto de Astronomía, AP 106, Ensenada 22800, BC, México; [croman@astro.unam.mx](mailto:croman@astro.unam.mx)

<sup>2</sup> Department of Physics and Astronomy, Vanderbilt University, VU Station 1807, Nashville, TN 37235, USA

<sup>3</sup> Department of Physics and Astronomy, Western Washington University, 516 High St., Bellingham, WA 98225, USA

<sup>4</sup> Centro de Astronomía (CITEVA), Universidad de Antofagasta, Av. Angamos 601, Antofagasta, Chile

<sup>5</sup> Departamento de Astronomía, Universidad de Concepción, Casilla 160-C, Concepción, Chile

<sup>6</sup> Max-Planck-Institute for Astronomy, Königstuhl 17, D-69117 Heidelberg, Germany

<sup>7</sup> Departamento de Astronomía, Facultad de Ciencias, Universidad de La Serena. Av. Juan Cisternas 1200, La Serena, Chile

<sup>8</sup> Center for Astrophysics and Space Astronomy, Department of Astrophysical and Planetary Sciences, University of Colorado, Boulder, CO 80309, USA

<sup>9</sup> Departamento de Astronomía, Facultad de Ciencias, Universidad de la República, Iguá 4225, 14000, Montevideo, Uruguay

<sup>10</sup> Departamento de Ciencias Físicas, Facultad de Ciencias Exactas, Universidad Andrés Bello, Fernández Concha 700, Las Condes, Santiago, Chile

<sup>11</sup> Vatican Observatory, V00120 Vatican City State, Italy

<sup>12</sup> Instituto de Física y Astronomía, Universidad de Valparaíso, Gran Bretaña 1111, Valparaíso, Chile

<sup>13</sup> Núcleo Milenio de Formación Planetaria, NPF, Universidad de Valparaíso, Chile

<sup>14</sup> Steward Observatory, Department of Astronomy, University of Arizona, 933 North Cherry Ave., Tucson, AZ 85721-0065, USA

<sup>15</sup> Department of Physics and Astronomy, The University of Western Ontario, 1151 Richmond St., London, ON N6G 1N9, Canada

<sup>16</sup> Department of Astrophysics, American Museum of Natural History, 79th Street at Central Park West, New York, NY 10024, USA

<sup>17</sup> Department of Physics, Davidson College, 405 N. Main St., Davidson, NC 28035, USA

<sup>18</sup> Instituto de Astronomía, Universidad Católica del Norte, Av. Angamos 0610, Antofagasta, Chile

<sup>19</sup> Centro de Investigación en Astronomía, Universidad Bernardo O'Higgins, Avenida Viel 1497, Santiago, Chile

<sup>20</sup> Universidad de La Laguna (ULL), Departamento de Astrofísica, E-38206 La Laguna, Tenerife, Spain

<sup>21</sup> Department of Astrophysical Sciences, 4 Ivy Lane, Princeton University, Princeton, NJ 08544, USA

<sup>22</sup> The Observatories of the Carnegie Institution for Science, 813 Santa Barbara St., Pasadena, CA 91101, USA

<sup>23</sup> Apache Point Observatory and New Mexico State University, P.O. Box 59, Sunspot, NM 88349-0059, USA

<sup>24</sup> Sternberg Astronomical Institute, Moscow State University, Moscow, Russia

Received 2022 January 20; revised 2022 November 13; accepted 2022 November 15; published 2023 January 11

## Abstract

The Sloan Digital Sky Survey IV APOGEE-2 primary science goal was to observe red giant stars throughout the Galaxy to study its dynamics, morphology, and chemical evolution. The APOGEE instrument, a high-resolution 300-fiber  $H$ -band (1.55–1.71  $\mu\text{m}$ ) spectrograph, is also ideal to study other stellar populations in the Galaxy, among which are a number of star-forming regions and young open clusters. We present the results of the determination of six stellar properties ( $T_{\text{eff}}$ ,  $\log g$ ,  $[\text{Fe}/\text{H}]$ ,  $L/L_{\odot}$ ,  $M/M_{\odot}$ , and age) for a sample that is composed of 3360 young stars, of subsolar to supersolar types, in 16 Galactic star formation and young open cluster regions. Those sources were selected by using a clustering method that removes most of the field contamination. Samples were also refined by removing targets affected by various systematic effects of the parameter determination. The final samples are presented in a comprehensive catalog that includes all six estimated parameters. This overview study also includes parameter spatial distribution maps for all regions and Hertzsprung–Russell ( $\log L/L_{\odot}$  vs.  $T_{\text{eff}}$ ) diagrams. This study serves as a guide for detailed studies on individual regions and paves the way for the future studies on the global properties of stars in the pre-main-sequence phase of stellar evolution using more robust samples.

*Unified Astronomy Thesaurus concepts:* [Young star clusters \(1833\)](#); [Pre-main sequence stars \(1290\)](#); [Star forming regions \(1565\)](#); [Fundamental parameters of stars \(555\)](#); [Near infrared astronomy \(1093\)](#)

*Supporting material:* figure sets, machine-readable table

## 1. Introduction

The complete characterization of the pre-main-sequence (PMS) phase of stellar evolution from low- to intermediate-

mass stars is an open problem in astrophysics. Various current models (e.g., Tognelli et al. 2011; Bressan et al. 2012; Baraffe et al. 2015; Dotter 2016) apply state-of-the-art theory in both the mainly convective and the mainly radiative stages of the PMS. Nevertheless, many processes are still to be considered when those models are compared to spectroscopic observations. For instance, accretion as a function of both mass and age, circumstellar emission, disk dust veiling of the stellar continuum, rotation, and the true chemical content of the youngest stellar populations are still absent from most models.

\* Based on SDSS Data Releases 16 and 17.



In order to produce better synthetic stellar atmosphere models that compare well to observed spectra of young stars, we require larger and better empirical libraries. Machine-learning automated classification provides the required muscle to process big data samples, but their results can only be as good as the input training samples. Thus, both supervised and unsupervised methods to determine PMS parameters require robust samples obtained in diverse star-forming regions. In turn, large enough samples are provided nowadays by large-scale spectroscopic surveys using fiber spectrographs capable of observing hundreds of targets simultaneously.

In optical wavelengths, the LAMOST survey (Zhao et al. 2012) has made important contributions to classifying spectra of young stars and to helping to classify young stars at other wavelengths (e.g., Fang et al. 2016, 2018, 2020). The Gaia-ESO survey (Gilmore et al. 2012) has provided insight into the chemical content, accretion, dynamics, and other properties in young star clusters (Bravi et al. 2018; Wright et al. 2019; Baratella et al. 2020, 2021; Bonito et al. 2020; Binks et al. 2021; Kos et al. 2021).

The Sloan Digital Sky Survey (SDSS) has hosted several focused studies based on multiobject spectroscopy of young stars and young star clusters in its third (SDSS-III; Eisenstein et al. 2011) and fourth phases (SDSS-IV; Blanton et al. 2017). A major advancement came in the infrared with the development of the SDSS-III APOGEE<sup>25</sup> (Majewski et al. 2017) and SDSS-IV APOGEE-2 programs (S. Majewski et al. 2022, in preparation). In the former, the IN-SYNC program produced a number of studies dedicated to classification of young star spectra and evolution of young stellar clusters (e.g., Cottaar et al. 2014, 2015; Foster et al. 2015; Da Rio et al. 2016, 2017). In the latter, a more ample APOGEE-2 survey of the Orion complex (Cottle et al. 2018) led to the first 6D (position–velocity) map of Orion using radial velocities and improved IN-SYNC parameters, as well as astrometric parameters from Gaia DR2 (Kounkel et al. 2018). APOGEE-2 data have also been used to provide classifications of O- and B-type stars in star-forming complexes in the 1–3 kpc distance range (e.g., Roman-Lopes et al. 2018; Borissova et al. 2019; Roman-Lopes et al. 2020a, 2020b; Ramírez-Preciado et al. 2020; Medina et al. 2021).

This study collects data from a majority of the star formation and young star cluster observations published in Data Releases 16 and 17 of the SDSS APOGEE-2 program. Our main goals are to overview and compare the extensive data and basic results obtained from the spectral classification and estimation of physical properties in 16 fields that include star formation complexes in the solar neighborhood ( $0.1 \text{ kpc} < d < 1 \text{ kpc}$ ) and the neighboring spiral arms ( $1 \text{ kpc} < d < 3 \text{ kpc}$ ).

The common goals in the study of these samples are (a) to identify the young star population, (b) to obtain reliable spectral classifications for young stars present, (c) to investigate the distribution of spectral properties ( $T_{\text{eff}}$ ,  $\log(g)$ ,  $[\text{Fe}/\text{H}]$ , luminosity, age, mass) among the young star populations, (d) to contribute to the characterization of the PMS stage by providing physical Hertzsprung–Russell (H-R) diagrams, and (e) to investigate how the spectral and physical properties of young stars relate to the evolution of young clusters, in terms of their circumstellar emission statistics.

This study relates various data sets with multiple parameters, which are presented in a collection of maps and diagrams. In view of this, we produced a number of Figure Sets that are available in the electronic version of the paper. Examples of such maps and diagrams for selected regions are presented as figures in the print version. The organization of the paper is as follows: In Section 2, we describe the generalities of the observed fields and spatial distribution of all targets. In Section 3, we describe our methodology to determine stellar parameters from the APOGEE near-infrared spectra, we present a selection of member candidates for each region using a clustering algorithm, and we discuss comparisons with other studies. In Section 4, we present the distribution and basic statistics of the parameters determined for each population. In Section 5, we present a short discussion on caveats—pertinent to our data—for the characterization of PMS populations. Finally, we summarize and discuss our work in Section 6.

## 2. Observations

The APOGEE and APOGEE-2 programs in SDSS used state-of-the-art fiber spectrographs, which use a circular field-of-view (FOV) radius and capacity for up to 300 simultaneous fiber observations. In a nutshell, fibers are plugged across a metal plate on the focal plane of the telescope, with target positions predrilled on the plate. As described in Wilson et al. (2019), the fibers are bundled for transmission to the bench spectrographs, where dispersed light is collected onto three near-IR detectors that divide each spectrum into three windows: blue 15145–15810 Å, green 15860–16430 Å, and red 16480–16950 Å (see Wilson et al. 2019, for details). One of the spectrographs is installed in the Northern Hemisphere (APOGEE-N), on the Apache Point Observatory 2.5 m Sloan telescope (Gunn et al. 2006), and the other one is located in the Southern Hemisphere (APOGEE-S), on the Las Campanas Observatory 2.5 m Du Pont telescope (Bowen & Vaughan 1973). The APOGEE-N and APOGEE-S instruments are nearly identical (Wilson et al. 2019), although some technical aspects at the telescope level are different. For instance, the FOV for the APOGEE-S instrument is smaller:  $0^{\circ}.95$  versus a  $1^{\circ}.5$  maximal FOV radius. At both telescopes, the plate system requires the use of a central post that blocks light in the field center, but whereas at APO the radius is  $1'.6$ , the one at LCO is  $5'.5$  for the on-axis acquisition camera and another region obscured for the off-axis guider camera. A more detailed description of the SDSS APOGEE instrumentation can be found in Wilson et al. (2019). Generalities of how fields and targets were assigned can be consulted in the APOGEE-2 general, APOGEE-2N, and APOGEE-2S targeting papers (Zasowski et al. 2017; Beaton et al. 2021; Santana et al. 2021). General spectral data processing is described in Nidever et al. (2015), with the APOGEE Stellar Parameters and Chemical Abundance Pipeline described in García Pérez et al. (2016). This paper makes use of reductions from Data Release 17, and the exact data handling is given schematically in Abdurro'uf et al. (2022), with the full descriptions in J. Holtzman et al. (2022, in preparation).

The core program in APOGEE and APOGEE-2 is a survey of all components of the Milky Way and some of the closest galaxies in the Local Group through *H*-band spectra of red giant stars. Young star samples come from a rather diverse series of short, alternative projects in various SDSS-IV APOGEE-2 subprograms. The targeting papers mentioned

<sup>25</sup> Apache Point Galactic Evolution Experiment.

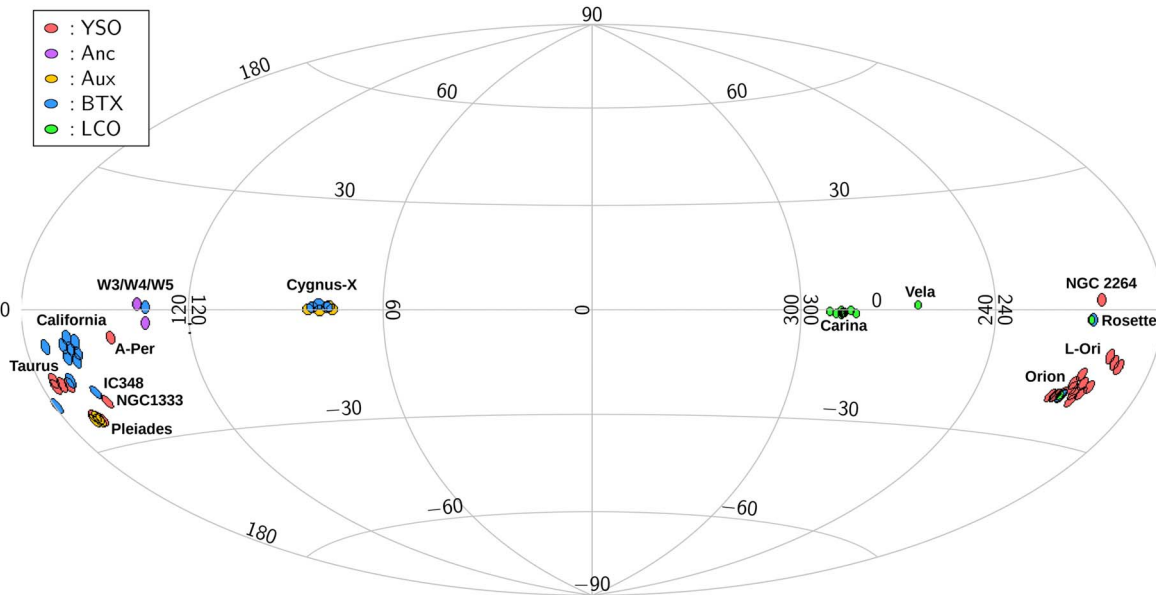


**Figure 1.** A map, in Galactic coordinates, showing the locations of all the fields listed in Table 3, along with labels identifying the 18 main regions reported in this study. Each circular field is projected with a realistic radius of 1.5 or 1°0 for regions observed with the APOGEE-N and APOGEE-S instruments, respectively. The colors of the fields refer to the field subprograms described in Section 2.

above contain a detailed description of all subprograms of the survey, with some aspects of subprograms given (Zasowski et al. 2017; Beaton et al. 2021; Santana et al. 2021). In Appendix B, we describe the specific APOGEE-2 subprograms that are relevant for our study.

The locations of all the corresponding APOGEE fields for this study are shown in Figure 1. Then, in Table 3 in Appendix A, we list the star formation and young cluster regions considered for the present overview. We list the assigned working names for the projects, the center coordinates of the APOGEE-2 fields observed for each project, and the APOGEE-2 subprogram category to which they pertain. We also list the total number of science targets observed in each field, prior to the candidate member selection. It is important to mention that for each field several 1 hr nominal integrations or “visits” are listed, using MJD as an identifier. Multiple visits were assigned to each field in all cases for several reasons: In the APOGEE program, a nominal 1 hr visit allows the instrument to achieve a signal-to-noise ratio ( $S/N$ )  $> 100$  for stars with  $H < 11.2$  mag. This is known as the “short” cohort. Medium (three summed, 1 hr visits) and large (six summed, 1 hr visits) cohorts allow us to achieve the  $S/N$  requirement for stars with brightness limits of 12.1 and 12.5 mag. It is worth noting, however, that in several of the star formation and young star cluster fields the targets in the large cohort were pushed down to  $H = 13$  mag because the  $S/N$  requirement for some scientific goals could be relaxed.<sup>26</sup> Therefore, for the programs described in this paper, the use of multiple visits is justified not only in terms of nominal brightness cohorts but also for other reasons, described as follows: (a) to reconfigure fibers to assign different targets in each visit—this way it was possible to observe a larger number of targets in crowded regions because the collision radius between fiber connectors limits the minimum separation to approximately 1' in the APOGEE-N

instrument and 85'' in the APOGEE-S instrument; (b) to allow us to observe embedded stars in regions of low to moderate extinction, down to  $H = 13$  mag; and (c) to investigate radial velocity (RV) variability, aimed, among other goals, to find and classify spectroscopic binaries.

In Figure 2 we show, as an example, a map of the Cygnus-X region where all APOGEE targets are laid out, along with the limits for each observed field. We indicate with a color table the  $S/N$  value for each target, showing values above 100 for a majority of sources, although reliable spectral classification and RV determinations can be obtained down to  $30 < S/N < 75$ . In Figure Set 2 we show similar maps for each of the main target regions, with color tables indicating  $S/N$ , as well as  $H$  magnitudes of the targets and the number of times (visits) a target was observed in order to achieve the desired  $S/N$  level depending on the brightness of the source.

The selection of target regions allows us to set common goals, in relation to the classification and characterization of young stars across a diverse set of local environments. In Appendix C, we provide some brief comments on particular regions in terms of individual science goals originally proposed for the various APOGEE internal projects. Several of the targets represent nearby ( $0.1 \text{ kpc} < d < 0.5 \text{ kpc}$ ) complexes or clusters dominated by low-mass star formation (e.g., Taurus, IC 348, Pleiades,  $\alpha$  Persei), while another group of regions (Cygnus-X, Carina, W3/W4/W5) can be classified as massive star-forming complexes outside the solar neighborhood ( $1 \text{ kpc} < d < 6 \text{ kpc}$ ). In a midrange group, regions like Orion, NGC 2264, or the Rosette are populations where massive stars are present but cannot be characterized as massive star-forming regions.

We must stress that conforming equivalent target samples across the diverse star-forming environments was not necessarily a goal that framed each APOGEE observational program. The paper by Cottle et al. (2018) details a complex selection function for the young stellar object (YSO) survey in APOGEE-2. For instance, the target selection for the Orion Nebula Cluster (ONC) was focused on the kinematic evolution

<sup>26</sup> For example, bright, massive stars at a distance of 2 kpc can be classified down to one spectral subtype using Brackett-11 and Brackett-13 lines, which can be well characterized with  $S/N > 60$  (Roman-Lopes et al. 2018).

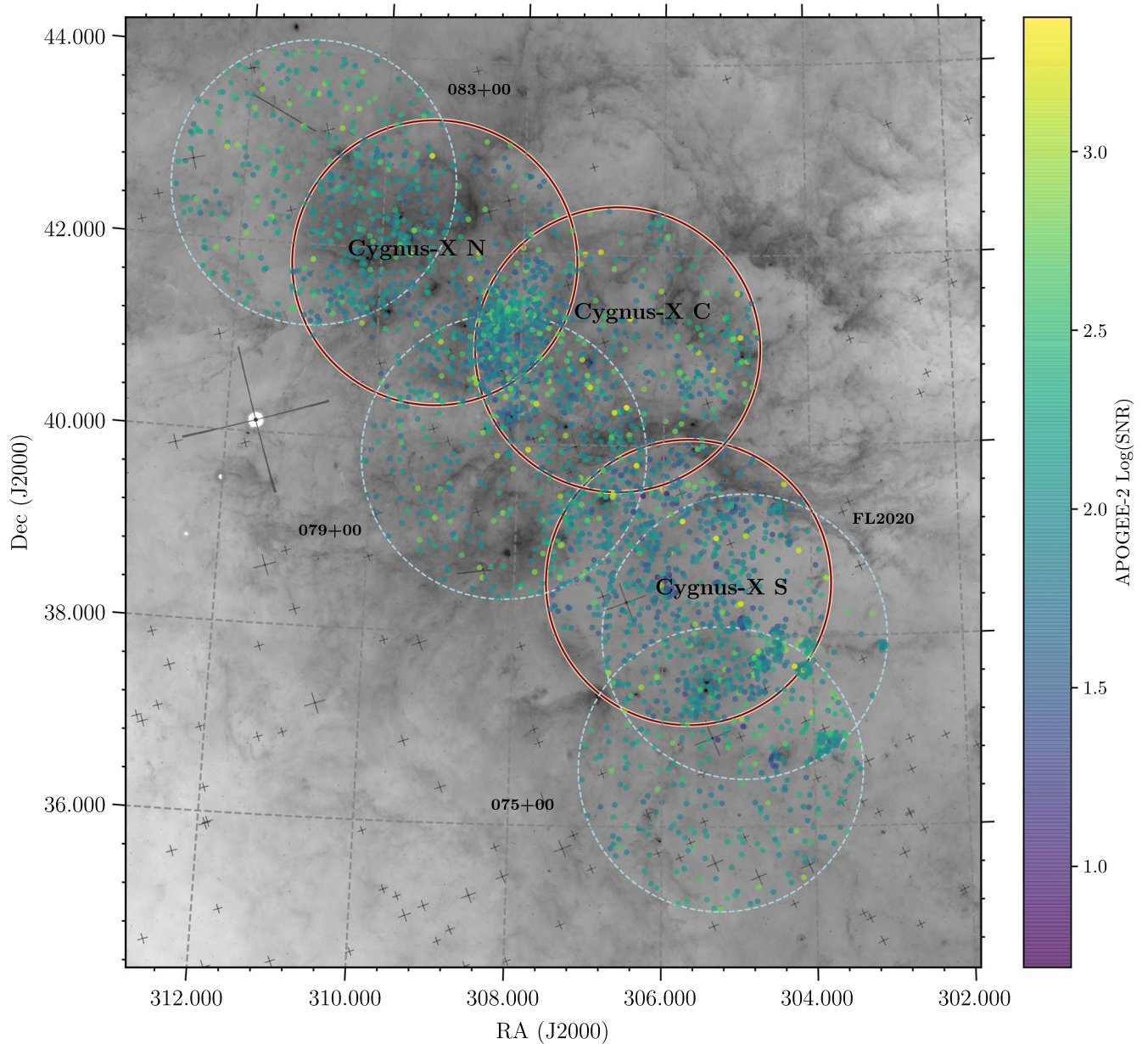


**Figure 2.** APOGEE-2 Cygnus-X complex fields are shown, delimited with circles; red circles indicate the main region fields, and the dotted blue circles indicate “auxiliary” fields (see Appendix B) also searched for candidate members. Colored filled circles indicate the positions of all scientific targets. The grayscale image in the background shows a  $12\ \mu\text{m}$  dust emission map from the WISE WSSA Atlas (Meisner & Finkbeiner 2014). The color bar indicates values of the S/N after visit combination. The component figures (42) for all the regions studied in this paper are available online in the Figure Set, which also include maps highlighting  $H$  mag brightness and number of visits.

(The complete figure set (42 images) is available.)

of the cluster; fields observed toward the Orion A cloud aimed mainly at the characterization of low-mass YSOs; then, observations of fields in the Orion OB1a and OB1b regions focus on study of the 5–10 Myr exposed groups that are evolving out from the cloud. The targets for those distinct populations were selected using lists of confirmed members from different authors to define loci in color–magnitude diagrams that were used to define candidate members, with additional candidates added using photometric variability as the main criteria. The resultant target lists, then, have to be filtered into brightness groups and run through a prioritization and collision radius avoidance algorithm, producing samples that

cannot be statistically complete in terms of spectral type or mass.

This last aspect is more notorious for massive star-forming region targets, where published lists of known members in the low mass range are less common than lists of OB members, and thus selecting low-mass YSO sources from photometric loci was more prone to field star contamination. It is also important to mention that for some regions, particularly those designed during the first 2 yr of the survey, the selection functions could not include distance estimations because Gaia parallaxes were not yet available. One clear example of this is W3/W4/W5, where low-mass young star candidate targets

were selected using only color–magnitude loci. As will be described in the next section, this unfortunately results in a large fraction of field contaminants. Using only photometric selections for candidate members produces a significant number of contaminants, as red giant stars can mimic the colors of embedded young sources. Moreover, even nearby regions like Taurus were significantly affected by the absence of parallax determinations during the selection function observed in the first visits.

Despite the heterogeneous nature of the sample, our methodology allows us to extract important information about diverse young stellar populations in an unprecedented collection of spectroscopic samples. This results in one of the largest catalogs of young stellar properties to date.

### 3. Methods

In this section we describe the processes used to determine six stellar parameters ( $T_{\text{eff}}$ ,  $\log g$ ,  $[\text{Fe}/\text{H}]$ ,  $\log L/L_{\odot}$ , mass, age) for the stars in the 16 regions described in the previous section. We describe a clustering method used to remove field population contaminants from the observed samples and display the results on maps where we show the distribution of the parameters for each region. Finally, we describe how the selection of members with significant infrared excess was done in order to find and classify, in rough evolutionary stages, those members with circumstellar emission via protoplanetary disks.

#### 3.1. Spectral Parameter Determinations with APOGEE Net II

The standard spectral analysis pipeline for the APOGEE core sample (Holtzman et al. 2015) is not adequate for the determination of spectral parameters in PMS low-mass stars (see Cottaar et al. 2014). For this reason, Olney et al. (2020) developed APOGEE Net, a data-driven approach to derive  $T_{\text{eff}}$ ,  $\log g$ , and  $[\text{Fe}/\text{H}]$  of stars observed with APOGEE. These authors have trained a deep convolutional neural network using previously derived parameters (or “labels”) for red giants and stars with  $T_{\text{eff}} > 4200$  K from “The Payne” pipeline (Ting et al. 2019), as well as parameters derived from photometric relations for the M- and K-type main-sequence dwarfs and PMS stars (for which “The Payne” could not derive reliable values). Furthermore, the neural network was trained on the estimates of  $T_{\text{eff}}$  and  $\log g$  for a sample of PMS stars, derived from interpolation of the photometry of such stars across PARSEC PMS isochrones (Bressan et al. 2012).

As the PMS estimates originally had a lot of scatter, the neural network was trained to replicate the effects of temperature on spectra from main-sequence dwarfs and the effects of surface gravity from giants. This way, APOGEE Net was able to refine the measurements of the parameters of PMS stars. It yielded self-consistent  $T_{\text{eff}}$  measurements (valid for stars with  $T_{\text{eff}} < 6500$  K), eliminating systematic gaps that were present in the earlier extractions, based mainly on cross-matching of the spectra against synthetic templates (e.g., Cottaar et al. 2014; Kounkel et al. 2018). Furthermore, it made it possible for the first time to measure  $\log g$  values calibrated to the isochrones, allowing this parameter to be used as a proxy for age. This has allowed independent confirmation that the spatial distribution of YSOs in the ONC depends strongly on the age of the stars, as was previously proposed by Beccari et al. (2017), with the older sources more distributed

throughout the ONC and the younger sources being predominantly concentrated near the Trapezium group.

APOGEE Net was expanded by Sprague et al. (2022), who complemented the training set by adding a comprehensive collection of  $T_{\text{eff}}$  and  $\log g$  estimates from the literature, allowing a consistent parameter determination across the H-R diagram, from late M to OB stars. This way, parameter determination is no longer limited to The Payne coverage and becomes self-consistent across the spectral type and luminosity class space. The Sprague et al. methods were applied to the entire APOGEE-2 target list, and the results we present in this study come from the most recent calibration of the neural network, named APOGEE Net II, which includes all sources from the SDSS DR16 (Ahumada et al. 2020) and DR17 (Abdurro’uf et al. 2022).

#### 3.2. Estimation of Physical Properties

For each of the regions, we obtained estimations of luminosities, masses, and ages, as well as visual extinction ( $A_V$ ), using an IDL-based code named `MassAge` (J. Hernández et al. 2022, in preparation). `MassAge` uses as input the  $T_{\text{eff}}$  estimates from the APOGEE Net II pipeline, geometric distance estimations from Bailer-Jones et al. (2021), and photometry from Gaia EDR3 (Gp, Rp, Bp) and the Two Micron All Sky Survey (2MASS;  $J$  and  $H$ ). The uncertainties in the estimated values are obtained using the Monte Carlo method of error propagation (Anderson 1976), assuming Gaussian distributions for the uncertainties in each of the input parameters.

The visual extinction,  $A_V$ , toward each source is estimated, along with a confidence range, by means of a Monte Carlo method that minimizes the differences between the extinction-corrected colors and the expected intrinsic colors from Luhman (2020). The observed colors are corrected using the extinction law of Cardelli et al. (1989), assuming a canonical interstellar reddening law (for simplicity we used  $R_V = 3.1$  for all regions). Luminosities are derived using the extinction-corrected  $J$  magnitude, the bolometric correction for PMS stars from Pecaut & Mamajek (2013), and Gaia EDR3 geometric distance estimations  $r_{\text{geo}}$  from Bailer-Jones et al. (2021). Finally, stellar masses and ages, plus confidence ranges, are obtained by means of Monte Carlo sampling and interpolation within the PARSEC-COLIBRI evolutionary model grid (Bressan et al. 2012) on the H-R diagram.

#### 3.3. Field Contamination Removal Using Density-based Clustering Methodology

As described in Section 2, a significant portion of the APOGEE targets are physically unrelated to the corresponding region. This is because the original target selection criteria were rather diverse for the different APOGEE programs. Therefore, it is necessary to apply a method to remove, as uniformly as possible, most field contaminants. Below we describe such a methodology. The method combines a clustering algorithm and distance cut refinements in order to narrow down our samples and generate final lists of *probable region members* (PRMs).

We chose the density-based clustering algorithm HDBSCAN (Campello et al. 2013) implemented under the R environment (R Core Team 2018) using the `hdbscan` library (Hahsler et al. 2019). The hierarchical nature of HDBSCAN allows us to detect stellar groups at different densities and discard points in locally nondense regions as noise. Given the vast diversity of regions explored, we needed a uniform scheme to globally isolate each

**Table 1**  
Sample Restrictions

Main Target Region	Restrictions	No. of Sources in Cut for Parameter Determination						$T_{\text{eff}}$ Limits, Age Cut
		$T_{\text{eff}},$ log $g$	[Fe/H]	log $L/L_{\odot}$	$M/M_{\odot}$	Age/Myr	RUWE > 1.4	
$\alpha$ Per	$33 < \mu/\text{mas yr}^{-1} < 36 \wedge 160 < r_{\text{geo}}/\text{pc} < 190$	122	69	98	98	95	28	3000, 6000
California	$5 < \mu/\text{mas yr}^{-1} < 10 \wedge 400 < r_{\text{geo}}/\text{pc} < 600$	29	16	29	29	25	9	3000, 5500
Carina	$5.8 < \mu/\text{mas yr}^{-1} < 7.8 \wedge 2.0 < r_{\text{geo}}/\text{kpc} < 3.0$	58	5	37	37	18	13	3500, 6000
Cygnus-X	$5.8 < \mu/\text{mas yr}^{-1} < 7.8 \wedge 0.9 < r_{\text{geo}}/\text{kpc} < 2.0$	340	3	269	269	152	46	3400, 6500
IC 348	$6.5 < \mu/\text{mas yr}^{-1} < 9.5 \wedge 280 < r_{\text{geo}}/\text{pc} < 340$	73	43	72	73	65	27	3600, 5500
NGC 1333	$10.5 < \mu/\text{mas yr}^{-1} < 13 \wedge 240 < r_{\text{geo}}/\text{pc} < 360$	69	59	67	67	40	50	3400, 5500
NGC 2264	$3.8 < \mu/\text{mas yr}^{-1} < 4.8 \wedge 600 < r_{\text{geo}}/\text{pc} < 800$	125	101	124	124	121	19	3400, 5500
$\lambda$ Ori	$1 < \mu/\text{mas yr}^{-1} < 5 \wedge 360 < r_{\text{geo}}/\text{pc} < 430$	223	172	222	222	212	68	3100, 5500
Orion A	$1 < \mu/\text{mas yr}^{-1} < 5 \wedge 360 < r_{\text{geo}}/\text{pc} < 430$	1095	884	1069	1069	994	307	3000, 5500
Orion B, front	$0.0 < \mu/\text{mas yr}^{-1} < 3.5 \wedge 340 < r_{\text{geo}}/\text{pc} < 370$	51	36	51	51	50	18	3000, 5500
Orion B, back	$0.0 < \mu/\text{mas yr}^{-1} < 3.5 \wedge 370 < r_{\text{geo}}/\text{pc} < 430$	227	192	224	224	209	61	3000, 5500
Orion OB1 front	$0.0 < \mu/\text{mas yr}^{-1} < 3.5 \wedge 320 < r_{\text{geo}}/\text{pc} < 370$	237	120	236	236	220	120	3000, 5500
Orion OB1 back	$0.0 < \mu/\text{mas yr}^{-1} < 3.5 \wedge 370 < r_{\text{geo}}/\text{pc} < 430$	72	28	72	72	66	82	3000, 5500
Pleiades	$47 < \mu/\text{mas yr}^{-1} < 52 \wedge 125 < r_{\text{geo}}/\text{pc} < 145$	293	168	212	212	177	0	3500, 5500
Rosette	$1.5 < \mu/\text{mas yr}^{-1} < 2.5 \wedge 1.0 < r_{\text{geo}}/\text{kpc} < 2.0$	163	30	136	136	90	26	3400, 5500
Taurus	$20 < \mu/\text{mas yr}^{-1} < 30 \wedge 120 < r_{\text{geo}}/\text{pc} < 170$	71	58	71	71	67	109	3400, 5500
Vela Ridge	$7.5 < \mu/\text{mas yr}^{-1} < 12.5 \wedge 0.8 < r_{\text{geo}}/\text{kpc} < 1.1$	194	95	178	1178	141	16	3400, 5500
W3/W4/W5	$0.0 < \mu/\text{mas yr}^{-1} < 2.5 \wedge 1.8 < r_{\text{geo}}/\text{kpc} < 2.2$	118	0	107	107	32	17	3500, 5700

environmental highest probable member list. The algorithm was applied to four dimensions of our catalog: Gaia proper motions ( $\mu_{\alpha}$ ,  $\mu_{\delta}$ ), Gaia parallax, and APOGEE Net log  $g$ . We use these parameters as the main discriminators because they combine high-quality astrometric information with the spectroscopically derived parameter that is most sensitive to young sources. HDBSCAN was fed with the uncorrelated principal components that preserved the data set variance at a 90% level.

We implemented the nearest-neighbor distance routine of the package under a Euclidean metric, imposing only a minimum number of cluster points of 20 sources (10 sources in the cases of California and NGC 2264), which works as a “smoothing” factor of the density estimates implicitly computed from HDBSCAN. As a result, three output parameters are produced for each source in each region’s initial catalogs: a data cluster number, membership probability, and outlier score. For most catalogs, the algorithm produced three data clusters, and four in a few cases.

### 3.4. Additional Parameter Restrictions

In Table 1 we list, for each region, a series of additional restrictions we applied to the HDBSCAN resultant samples. Restrictions are applied for the astrometric dimensions and at the six stellar parameters.

We cover regions within a considerable range of distances (0.1–4.1 kpc on average). As mentioned by Hunt & Reffert (2021), distant regions are difficult to separate from field stars, as proper motions and parallaxes become decreasingly informative at large distances. The Gaia geometric distance ( $r_{\text{geo}}$ ) errors increase from tens to hundreds of parsecs as we move from nearby (0.1–0.5 kpc) to distant complexes (1–4 kpc). This way, as distance increases, HDBSCAN is more prone to confuse members as field sources, assigning low-probability membership or high outlier scores to them. At larger distances, confusion by overlapping sources and multiple components along the line of sight also increases. In order to mitigate this,

we removed from the catalogs all sources with Gaia RUWE values larger than 1.4 (Lindegren et al. 2018). In addition, we used  $A_V$  versus  $r_{\text{geo}}$  plots to determine whether the membership probabilities converged well for a specific group. Initially, we considered that PRMs should typically lie on a narrow horizontal band—a co-distant object layer—that may form above a certain extinction threshold value. In Figure 3 we show an example of the derived group distribution for the region  $\lambda$  Ori in the geometrical distance ( $\langle r_{\text{geo}} \rangle$ ) versus  $A_V$  plot. Most sources with HDBSCAN membership probability values above 0.6 coincide well with most co-distant sources in the best-defined group, but we show also how some objects with low membership scores also coincide with the co-distant object layer. Thus, for each catalog, we define ranges in distance and total proper motion ( $\mu = \sqrt{\mu_{\alpha}^2 + \mu_{\delta}^2}$ ) that contain the co-distant object layer, and in this way we are able to include a few more sources in each sample that fall within that distance, even if they have low membership scores. This criterion removes additional contaminants from the group of interest while including possible PRMs that could end in other groups owing to the nuisances of the clustering algorithm.

The reliability of the six main parameters depends strongly on both the population environment and the spectral type. It is not trivial to take into account the diversity of conditions the young star groups are subject to, particularly the nonuniform extinction. Spectral classification from APOGEE data is particularly difficult for late M types, where the fit of the continuum is complicated by the overabundance of atomic lines. For early types above solar, model degeneracy from PMS to main sequence and non-LTE effects rapidly become notorious, resulting in large discrepancies in the spectral-type-to- $T_{\text{eff}}$  conversion used for the neural network training samples. In addition, the isochrone/constant mass line grid across the H-R diagram is far from regular, which complicates determination of physical parameters, especially for the earlier types and for sources falling close to the edges of the isochrone

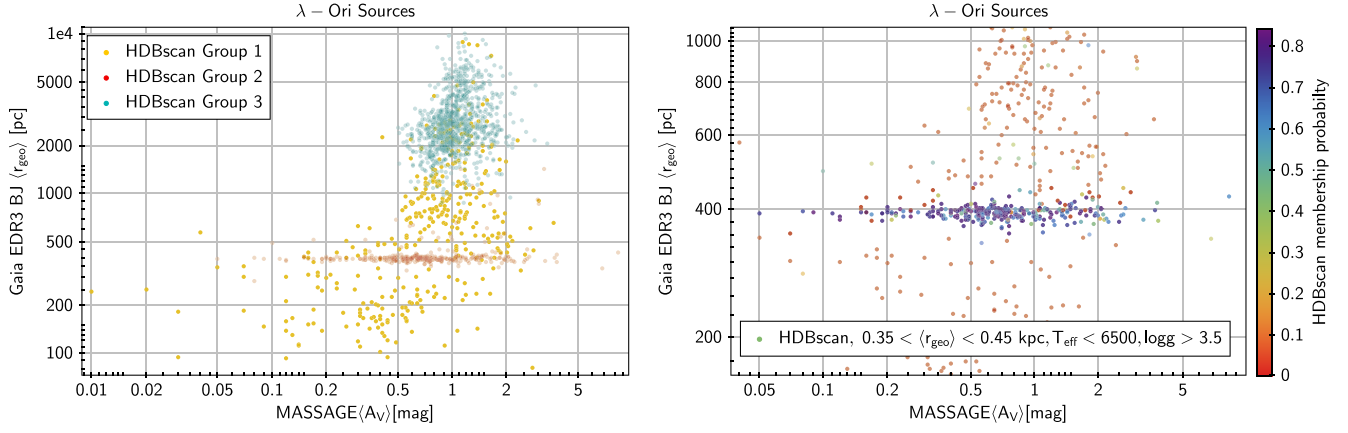


**Figure 3.** Example of region member selection refinements. Both panels show a distribution of the geometric distance estimates from Bailer-Jones et al. (2021) vs. mean extinction,  $\langle A_V \rangle$ , from `MASSAGE`. The left panel shows the HDBSCAN resultant cluster groups for all targets observed in the  $\lambda$  Ori region, where it can be seen how Group 2 stars contain most of the sources coinciding with the expected distance to the cluster (about 380 pc), stars from Group 3 are in most cases background field sources, and Group 1 may contain a few sources at the expected distance. In the close-up in the right panel, the colors of the points indicate the cluster membership probability, where the stars with bluer colors pertain to a group that contains stars from Groups 1 and 2 with distances between 350 and 450 pc,  $\log g > 3.5$ , and  $T_{\text{eff}} > 6500$ . Those restrictions define the HRMs for this region.

**Table 2**  
HRM Median Values per Region<sup>a</sup>

Region	$T_{\text{eff}}/\text{K}$	$\log g$	[Fe/H]	$\log L/L_{\odot}$	$M/M_{\odot}$	Age/Myr
$\alpha$ Per	$3602 \pm 371$	$4.5 \pm 0.13$	$0.0 \pm 0.03$	$-1.3 \pm 0.42$	$0.5 \pm 0.15$	$51.8 \pm 14.1$
California	$3917 \pm 387$	$4.2 \pm 0.18$	$-0.1 \pm 0.03$	$0.0 \pm 0.37$	$0.6 \pm 0.20$	$2.7 \pm 1.7$
Carina	$4903 \pm 545$	$3.9 \pm 0.18$	...	$0.8 \pm 0.25$	$1.7 \pm 0.86$	$1.5 \pm 1.1$
Cygnus-X	$5420 \pm 426$	$4.2 \pm 0.14$	...	$1.0 \pm 0.17$	$2.3 \pm 0.34$	$1.4 \pm 0.8$
IC 348	$3878 \pm 233$	$4.0 \pm 0.11$	$0.0 \pm 0.02$	$-0.3 \pm 0.28$	$0.7 \pm 0.08$	$3.5 \pm 1.9$
NGC 1333	$3536 \pm 219$	$3.8 \pm 0.13$	$0.0 \pm 0.02$	$-0.7 \pm 0.39$	$0.5 \pm 0.10$	$3.2 \pm 2.3$
NGC 2264	$3723 \pm 187$	$4.3 \pm 0.15$	$0.0 \pm 0.03$	$-0.5 \pm 0.19$	$0.7 \pm 0.08$	$3.5 \pm 1.8$
$\lambda$ Ori	$3727 \pm 186$	$4.1 \pm 0.14$	$0.0 \pm 0.02$	$-0.4 \pm 0.23$	$0.6 \pm 0.09$	$3.0 \pm 1.4$
Orion A	$3642 \pm 177$	$4.0 \pm 0.16$	$0.0 \pm 0.02$	$-0.4 \pm 0.23$	$0.6 \pm 0.10$	$2.6 \pm 1.4$
Orion B, front	$3669 \pm 151$	$4.1 \pm 0.09$	$0.0 \pm 0.02$	$-0.5 \pm 0.22$	$0.7 \pm 0.06$	$4.2 \pm 2.6$
Orion B, back	$3667 \pm 178$	$3.9 \pm 0.14$	$0.0 \pm 0.02$	$-0.3 \pm 0.24$	$0.5 \pm 0.09$	$1.5 \pm 0.7$
Orion OB1, front	$3973 \pm 329$	$4.3 \pm 0.15$	$0.0 \pm 0.02$	$-0.4 \pm 0.22$	$0.7 \pm 0.11$	$4.7 \pm 1.9$
Orion OB1, back	$4243 \pm 446$	$4.2 \pm 0.15$	$0.0 \pm 0.03$	$-0.2 \pm 0.25$	$0.8 \pm 0.21$	$4.1 \pm 1.8$
Pleiades	$3873 \pm 481$	$4.6 \pm 0.08$	$0.0 \pm 0.02$	$-1.1 \pm 0.47$	$0.6 \pm 0.15$	$87.6 \pm 37.6$
Rosette	$4418 \pm 352$	$4.0 \pm 0.17$	$-0.1 \pm 0.04$	$0.4 \pm 0.26$	$0.9 \pm 0.30$	$1.1 \pm 0.4$
Taurus	$3552 \pm 241$	$4.1 \pm 0.14$	$0.0 \pm 0.03$	$-0.6 \pm 0.23$	$0.5 \pm 0.13$	$2.9 \pm 1.4$
Vela	$4010 \pm 353$	$4.1 \pm 0.16$	$0.0 \pm 0.03$	$-0.1 \pm 0.30$	$0.7 \pm 0.19$	$2.5 \pm 1.5$
W3/W4/W5	$5265 \pm 475$	$4.0 \pm 0.16$	...	$1.3 \pm 0.27$	$2.6 \pm 0.51$	$1.3 \pm 0.7$

**Note.**

<sup>a</sup> Targets with multiple observations were averaged for analysis. Values listed correspond to median and median absolute deviation, except for age values in Cygnus-X, Carina, and W3/W4/W5, where we used simple mean values.

grid. For all these reasons, in order to provide catalogs with reliable parameters, we decided to further limit our samples according to conservative yet safer cuts.

We started by restricting  $T_{\text{eff}}$  to values below 7000 K and  $\log g$  to values above 3.0. The first cut prevents us from using underestimated temperatures of intermediate- to high-mass sources. The second cut removes a majority of field evolved-star contamination.

In the final catalogs, we include only estimates of luminosity and mass for sources with  $T_{\text{eff}} < 6500$  K, as we found that the interpolation method of `MASSAGE` is optimal below that value. As for age estimations, mass versus age plots for all the samples show that sources for which the interpolation is performed near the edges of the isochrone/constant mass line grid tend to group in a false sequence, while correctly interpolated values lie below that sequence. In addition, for

some regions, sources within the lowest  $T_{\text{eff}}$  bins could have overestimated values that, in turn, would bias the sample toward large age values. The last column in Table 1 shows the  $T_{\text{eff}}$  values used in each sample in order to retain only those sources with reliable age estimates. In IC 348, NGC 1333, and Taurus, we also removed stars with  $\log L/L_{\odot} < -1.0$  from `MASSAGE` in order to remove overestimated  $T_{\text{eff}}$  values from the catalog. In Table 2 we list median values and their corresponding median absolute deviation for the six main parameters in each region.

### 3.5. Separation of Front and Back Populations in Orion B and Orion OB1

In the case of the Orion B and Orion OB1 samples, we noticed that both restricted samples, a plot of extinction versus

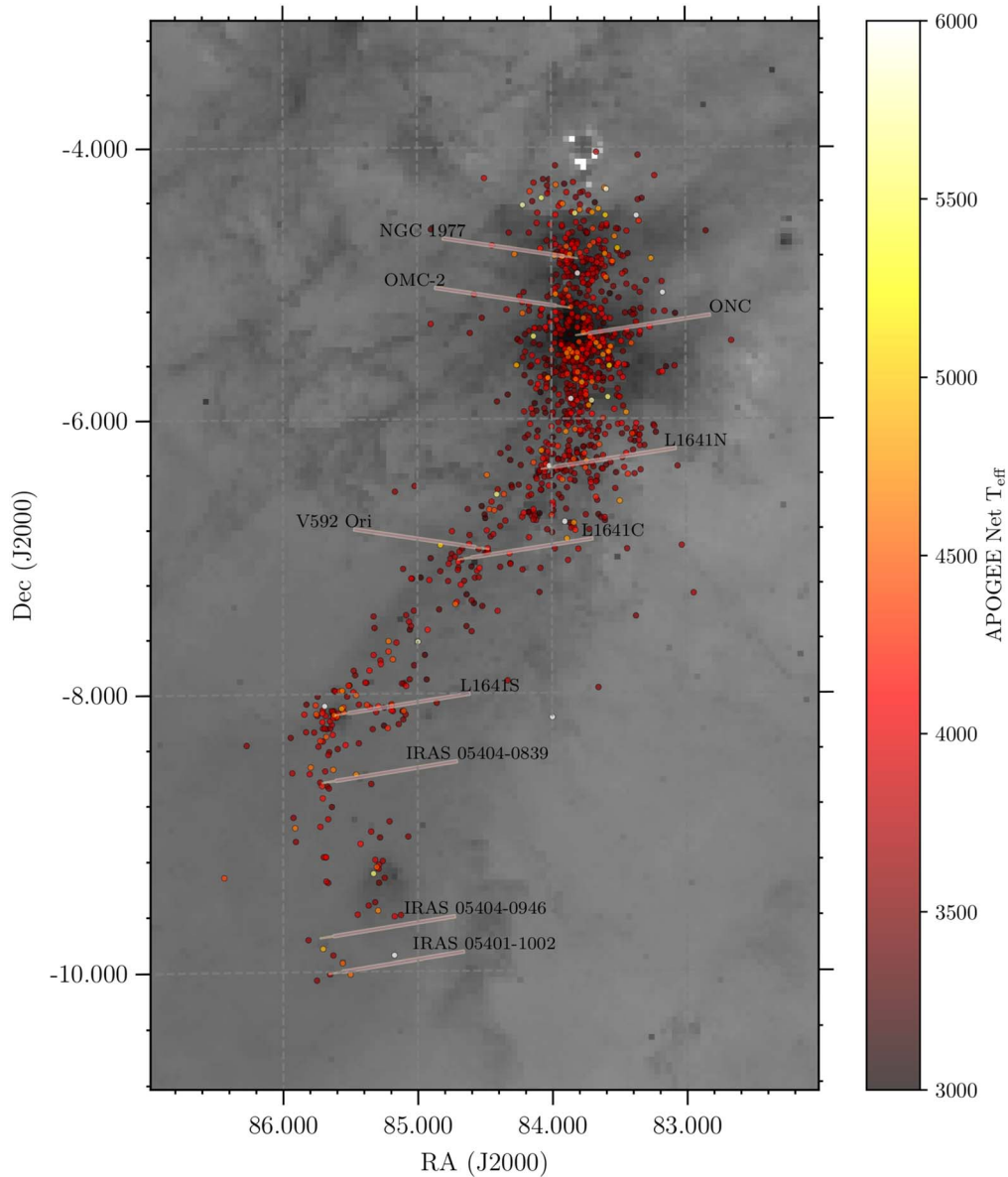


**Figure 4.** A map of the Orion A region, showing the  $T_{\text{eff}}$  determined for APOGEE-2 targets using APOGEE Net. Colored filled circles indicate the positions of all scientific targets. The grayscale image in the background shows a  $12\ \mu\text{m}$  dust emission map from the WISE WSSA Atlas (Meisner & Finkbeiner 2014). The color bar indicates  $T_{\text{eff}}$ . All the component figures (93) for the 17 regions studied in this paper are available online in the Figure Set, including maps highlighting  $\log g$ ,  $[\text{Fe}/\text{H}]$ , stellar mass, stellar age, and luminosities.

(The complete figure set (93 images) is available.)

distance, showed a clear minimum in the density of sources at  $r_{\text{geo}} \sim 370\ \text{pc}$ . This is consistent with the studies of Briceño et al. (2019) and Hernández et al. (submitted). For this reason, we decided to divide those samples into two groups, one with  $340 < r_{\text{geo}}/\text{pc} < 370$  (named “front”) and another one with  $370 < r_{\text{geo}}/\text{pc} < 430$  (named “back”). The groups are listed separately in Tables 1 and 2, and they are also shown with distinct symbols in the maps of Figure Sets 1 and 2 in Appendix E.

#### 4. Results

Applying the above selection criteria, a total of 3360 PRM sources were considered for further analysis (this is the sum of the number of sources for which  $T_{\text{eff}}$  and  $\log g$  were determined for each region, as listed in the third column of Table 1). In

Table 4, Appendix D, we present a master table listing that includes identifications, positions, geometric distance, visual extinction, and the values of the six main parameters determined in this paper:  $T_{\text{eff}}$ ,  $\log g$ ,  $[\text{Fe}/\text{H}]$ , mass, age, and luminosity.

##### 4.1. Parameter Maps and Distributions

The PRM lists were used to map the distributions of the six main parameters. In Figure 4 we show, as an example, the  $T_{\text{eff}}$  distribution in the Orion A complex. These maps provide an unprecedented overview of the properties of solar- and subsolar-type young stars in three kinds of star-forming regions: (a) nearby ( $d < 0.4\ \text{kpc}$ ) complexes predominantly forming low-mass stars, (b) intermediate-distance ( $0.4\ \text{kpc} < d < 1.5\ \text{kpc}$ ) complexes with a moderate content of

massive stars, and large star-forming complexes with significant massive star content in the neighbor spiral arms ( $d > 1.5$  pc), all obtained with the same type of instrument and using the same processing for the resulting data sets. The online figure set contains similar maps for all 16 regions.

#### 4.1.1. Landmark Labels

The target maps and the parameter spatial distribution maps were constructed using as background image cuts from the Wide-field Infrared Survey Explorer (WISE) WSSA  $12\ \mu\text{m}$  dust emission Atlas (Meisner & Finkbeiner 2014). The  $12\ \mu\text{m}$  dust emission delineates with great clarity both molecular cloud and photodissociation regions in each map, without adding too much confusion from bright stellar sources or features (some extremely bright stars leave a visible residual mark). However, in those maps it is difficult to assess the location of young star clusters associated with current episodes of stellar birth. In addition, most of those episodes in our regions are well characterized in the literature. We added the locations of known embedded clusters and groups listed in several catalogs: for the California, NGC 2264, Orion A, and Orion B regions, we used the catalog of Porras et al. (2003); for the Cygnus-X, IC 348, NGC 1333, and Taurus regions, we used the catalog of Bica et al. (2003); for the Carina,  $\lambda$  Ori, and W3/W4/W5 regions, we used the catalog of Avedisova (2002); in the case of the Rosette complex, we used the cluster list of Cambrésy et al. (2013); for the remaining regions,  $\alpha$  Per, Pleiades, Orion OB1, and Vela, we collected locations of known groups directly from the SIMBAD astronomical database (Wenger et al. 2000).

#### 4.2. Hertzsprung–Russell Diagrams

We used the derived parameters to construct, for each region, H-R (luminosity versus  $T_{\text{eff}}$ ) diagrams. Examples of these diagrams for two regions are shown in Figure 5. The  $\log g$  values were added with a color scale. Symbols are marked according to the parameter restrictions described in the previous section. In all the plots we show isochrone and constant mass curves obtained from the PARSEC-COLIBRI evolutive models (Bressan et al. 2012).

It is clear from these diagrams that APOGEE Net and *MassAge* provide highly reliable stellar parameters for nearby regions, helped by very precise Gaia parallaxes and low column densities (see the example of the H-R diagram for the Pleiades). However, for the most distant regions located outside our local Galactic spiral arm, current Gaia distance uncertainties increase to hundreds of parsecs. In those regions we are also dealing with overlapping clouds and consequently highly variable extinction. For these reasons, the extinction is likely to be underestimated for many distant sources, and the resultant *MassAge* luminosities are more uncertain. See Section 5 for a more detailed discussion on the H-R diagrams for the different regions.

#### 4.3. Average Metal Abundance

In most regions, the average metal abundance,  $[\text{Fe}/\text{H}]$  from the APOGEE Net II tables, appears to have a mostly uniform behavior around solar values for sources with  $T_{\text{eff}} < 4000$  K. Above this value, the parameter dispersion increases significantly. The effect is more notorious for samples in the more distant regions like Carina, W3/W4/W5, and Cygnus-X. Olney et al. (2020) discussed how the APOGEE Net algorithm

tends to predict lower values of  $[\text{Fe}/\text{H}]$  for hotter stars, but their test samples were smaller and limited to nearby regions, so we confirm this bias with the larger samples used in this study.

## 5. Discussion

One of the main results of this study is the compilation of a significant catalog of stellar properties for young stars in a collection of star-forming regions around the Sun, which is presented in Table 4. However, our analysis also helps to evince how the characterization of young star populations poses a number of complications that are not necessarily exclusive of this paper, which are important to consider, as similar studies will arise for similar data sets and similar techniques in big-data treatments.

*Metal abundance.*—Methods that compare observed spectra with synthetic models are based on the goodness of fit of groups of metal lines present on the spectral window. Stars of higher  $T_{\text{eff}}$  have fewer lines, and stars with larger rotation velocities have broader lines, which may propose stars with lower  $[\text{Fe}/\text{H}]$  as better fits for early-type sources or rapid rotators. Nonintrinsic variations of the  $[\text{Fe}/\text{H}]$  parameter as a function of temperature are not exclusive of APOGEE data; for instance, this was also discussed by Kos et al. (2021) in optical spectra from the GALAH survey.

By limiting our samples to  $T_{\text{eff}} < 4000$  K, the data sets are reduced but are much more reliable. This way, the APOGEE Net II data confirm that star-forming regions in the solar neighborhood have solar abundance (see Table 2), which is in agreement with recent studies such as those of Spina et al. (2014) or Kos et al. (2021). In Table 2 we show how the median values of the APOGEE Net II  $[\text{Fe}/\text{H}]$  label for sources with  $T_{\text{eff}} < 4000$  K are all dead centered on solar for all regions except Carina, Cygnus-X, and W3/W4/W5, with no reliable samples in that  $T_{\text{eff}}$  range. It is not expected that star-forming regions present significant deviations from solar abundance within a few kiloparsecs from the Sun (Spina et al. 2017); our most distant remaining samples are in NGC 2264, Vela, and the Rosette in the 1 kpc range, all showing a solar value as well.

*Age determination.*—The APOGEE Net II neural network produced stellar parameters across the entire H-R diagram, and it has been optimized to consider the spectrophotometric properties of young stars (Olney et al. 2020; Sprague et al. 2022). However, as we mentioned in Section 3.4, APOGEE Net II  $T_{\text{eff}}$  values in some of the regions may not be precise enough above 7000 K and below 3400 K, affecting the estimation of masses and ages with the *MassAge* routines.

In addition, we have to consider that the determination of young cluster ages also includes some model-dependent issues. Due to the close distance and minimal extinction toward this cluster, our Pleiades sample presents uniform quality within the  $0.4\text{--}1\ M_{\odot}$  range and forms a tight sequence running slightly above the 100 Myr PARSEC-Colibri isochrone. The expected age for this cluster is 110–160 Myr (Gossage et al. 2018), but the median age we obtain is  $88 \pm 38$  Myr. In Figure 6 we show a comparison of the Gaia  $B_P - R_P$  colors and APOGEE  $T_{\text{eff}}$  values with those listed in the empirical sequence of Esplin et al. (2018); we can see how the differences between the empirical and observed sequences are very small. However, these small color or  $T_{\text{eff}}$  differences translate as dispersion in the individual age estimations with *MassAge*. The PARSEC-Colibri isochrone curves between 30 and 100 Myr have

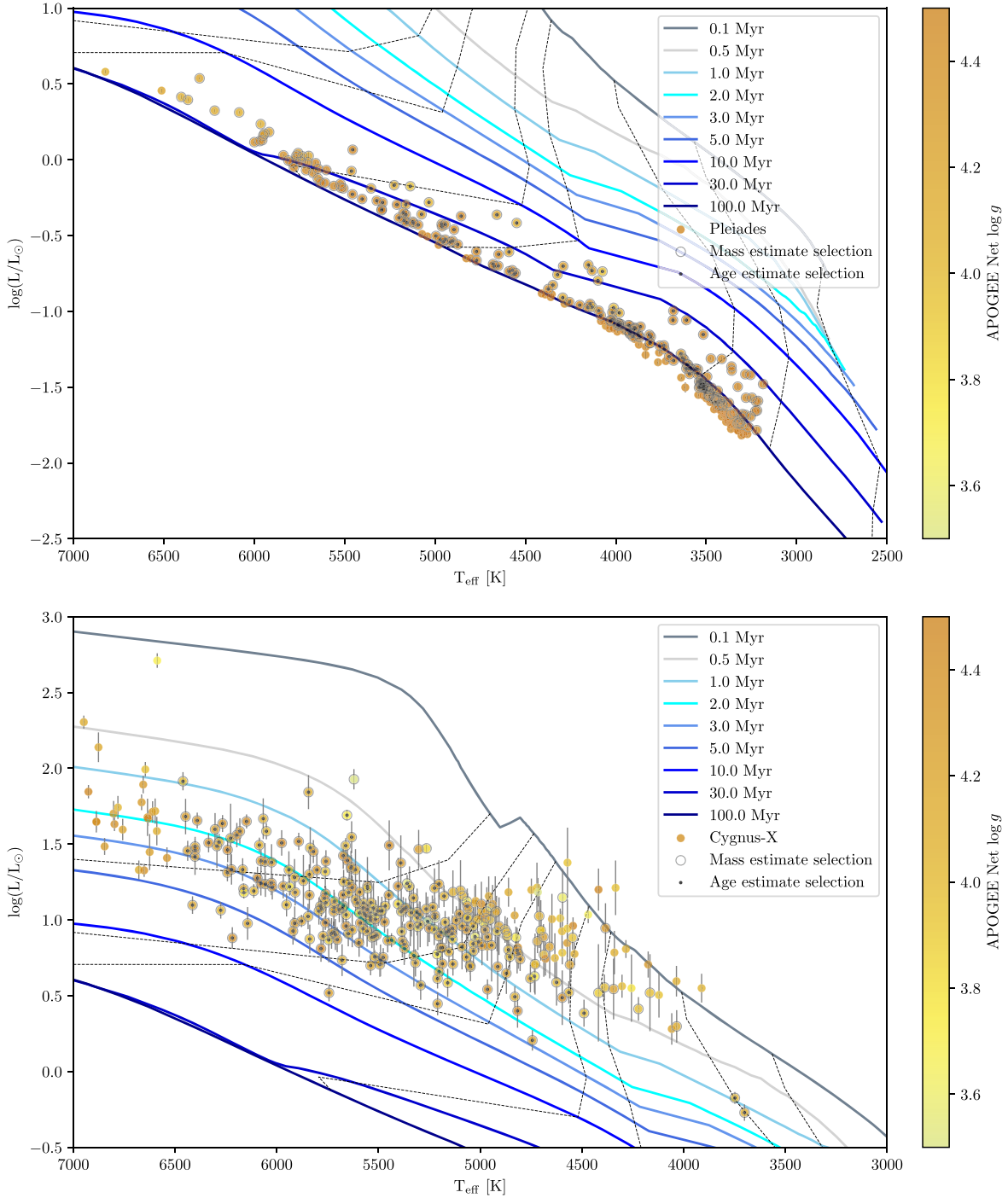


**Figure 5.** Example H-R diagrams for the Pleiades (top) and Cygnus-X regions (bottom). In the diagrams, solid curves are PARSEC-COLIBRI PMS isochrones at 0.1, 0.5, 1.0, 2.0, 3.0, 5.0, 10, 30, and 100 Myr, while the dashed curves indicate constant mass locus for models of 0.1, 0.3, 0.5, 0.8, 1.0, 1.5, 2.0, 3.0, and 5.0  $M_{\odot}$ . All the diagrams for the 16 regions studied in this paper are available online in the Figure Set. It contains 16 components.

(The complete figure set (16 images) is available.)

separations barely larger than our bolometric luminosity estimations, and if we compare to other isochrone models, like MIST (Dotter 2016), we will obtain a different set of values because the isochrone tracks do not run sufficiently close to each other to predict ages with nonsignificant discrepancies. Age uncertainties of a few tens of megayears are actually typical for clusters of similar age to the Pleiades (e.g., Caiazzo et al. 2020). As we go to younger ages, the discrepancies may increase, as warned by the MIST group

themselves (Choi et al. 2016), who expressed the need for better modeling of the PMS and low main sequence.

## 6. Summary and Future Work

The SDSS-III APOGEE and SDSS-IV APOGEE-2 programs represent one of the most important near-infrared large-scale spectroscopic surveys aimed at reconstructing the evolution history of the Milky Way. A fraction of the survey telescope

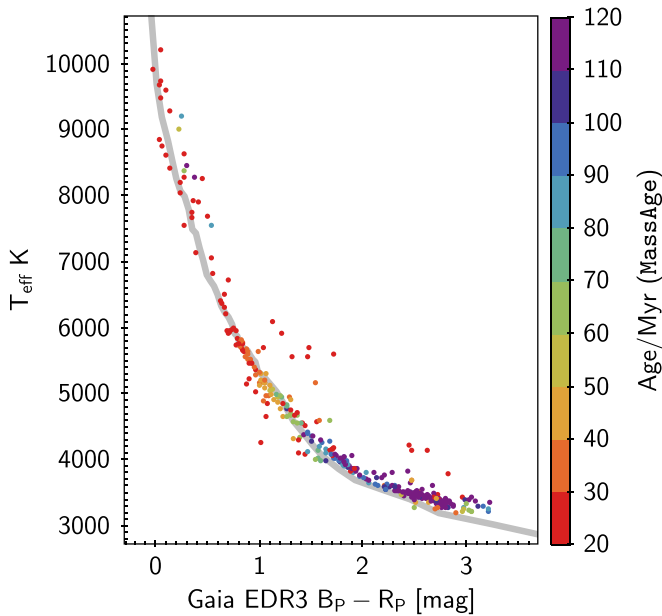


**Figure 6.** Effective temperature vs. Gaia EDR3 colors for the APOGEE Pleiades sample. The symbol colors represent age estimates from *MassAge*. The solid line is the empirical sequence from Esplin et al. (2018).

time was dedicated to the development of key scientific goals, one of them being the study of young stellar populations in a number of nearby ( $d < 500$  pc) low-mass star-forming complexes and several massive star-forming complexes in the local and neighbor spiral arms ( $1 \text{ kpc} < d < 3 \text{ kpc}$ ). This paper compiles and describes data for 16 star-forming regions surveyed as part of the APOGEE and APOGEE-2 programs. It provides a common analysis across all data sets, including the determination of spectroscopic parameters ( $T_{\text{eff}}$ ,  $\log g$ ,  $[\text{Fe}/\text{H}]$ ) through the APOGEE Net II neural network (Sprague et al. 2022) and the estimation of three additional parameters ( $L/L_{\odot}$ , stellar mass, age) through interpolation of PMS evolutionary models (Bressan et al. 2012) using a code named *MassAge* (J. Hernández et al. 2022, in preparation). We constructed H-R diagrams for high-probability members of all regions.

We developed a simple method to extract, from the original data sets for each region, the sources that are most probable to be physically associated with the very young, sometimes actual star-forming region. This was necessary because the initial lists of targets for each APOGEE program or set of visits were selected for rather diverse scientific goals and following different criteria. We applied a method to remove, as uniformly as possible, most field contaminants or objects that are nonmembers of the respective region. The method combines the application of a clustering algorithm (based on *HDBSCAN*) followed by distance cut refinements. Among the data considered are distances and proper motions from Gaia, combined with available photometry and, for specific regions, other ad hoc conditions. The result was the creation of working samples made of probable members for each region of study. All these constitute a reliable database that allowed us to apply consistently a common methodology.

Our analysis shows that APOGEE Net II reliably provides average abundance estimates for late-type stars, but such estimates are systematically less reliable for  $T_{\text{eff}} > 4500$  K. The Gaia-based distances increase in uncertainty for regions beyond the solar neighborhood, affecting the determination of

bolometric luminosities for star-forming complexes in the 1–2 kpc range. In turn, this also affects the estimation of age and mass. We provided a brief discussion of the spatial parameter distributions, H-R diagrams, and the circumstellar disk candidate content for each region. The most important contribution of this general analysis is that we are able to put on the table serious complications that are still present in the characterization of the PMS stage of stellar evolution, despite using a very robust sample of excellent quality, and despite using the most precise parallax determinations to date.

APOGEE Net II offers a robust methodology that also has the advantage of being reasonable in terms of computing cost. But it is important that we keep revising the precision of the method, given the complications that arise from the characteristics of stars during the PMS. For instance, the presence of circumstellar disks, strong chromospheric activity, accretion, and other aspects, such as deviations from local thermodynamic equilibrium at earlier spectral types, are still to be accounted for in synthetic models. At this point, while we still work in a limited parameter space, we can learn from the comparison with other data sets and methods. Currently, some of those methods are being directly applied to APOGEE data, like the Gradient Tree Boosting heuristic parameter assignment of Mejía-Narvaez et al. (2022), the Asexual Genetic Algorithm (L. Adame et al. 2022, in preparation), or other machine-learning methods like The Payne (Ting et al. 2019) or The MWM-Payne (I. Straumit et al., submitted). The Milky Way Mapper will provide a much larger sample of young star spectra that will increase the robustness of statistics and will reduce the uncertainties to a level where parameters like accretion, continuum veiling, and others associated with the PMS can reliably be incorporated into models. Samples like those presented in this study are a solid starting point.

One dedicated large-scale survey of embedded populations in star-forming regions, young star clusters, distributed young stars, and OB associations is still missing from the overall picture. The fifth phase of the SDSS (SDSS-V) is programmed to perform such a survey as part of the goals of the Milky Way Mapper project (Kollmeier et al. 2017), promising a much-needed large-scale perspective and the volume required for robust statistical studies that will serve to narrow down the observational uncertainties and, finally, constrain PMS evolution models. Along with the capital contribution of Gaia astrometric parameters (Gaia Collaboration et al. 2016) for large samples of sources in all Galactic environments and the increasing availability of synoptic data, we are opening a new chapter in the study of young stars, where a precise description of the PMS evolution and a deep understanding of the kinematics of young stellar clusters are clearly feasible.

The authors want to acknowledge the help of an anonymous referee, whose comments and suggestions helped us to improve the content of our manuscript. C.R.-Z. acknowledges support from projects CONACYT CB2018 A1S-9754, Mexico and UNAM DGAPA PAPIIT IN112620, Mexico. J.H., M.T., and J. S. acknowledge support from CONACYT project No. 86372 and the UNAM-DGAPA-PAPIIT projects IA102921, IN110422, and IN107519, Mexico. R.L.-V. acknowledges support from a posdoctoral fellowship from program “Estancias Posdoctorales por México,” CONACYT. D.M. is supported by ANID BASAL project FB210003. K.P.R. acknowledges support from ANID FONDECYT Iniciación

11201161. D.A.G.H. acknowledges support from the State Research Agency (AEI) of the Spanish Ministry of Science, Innovation and Universities (MCIU) and the European Regional Development Fund (FEDER) under grant AYA2017-88254-P. A.S. gratefully acknowledges support from the Fondecyt Regular (projectcode 1220610), from ANID BASAL projects ACE210002 and FB210003, and from the Chilean Centro de Excelencia en Astrofísica y Tecnologías Afines (CATA) BASAL grant AFB-170002. J.G.F.-T. gratefully acknowledges the grant support provided by Proyecto Fondecyt Iniciación No. 11220340, from ANID Concurso de Fomento a la Vinculación Internacional para Instituciones de Investigación Regionales (Modalidad corta duración) Proyecto No. FOVI210020, from the Joint Committee ESO-Government of Chile 2021 (ORP 023/2021), and from Becas Santander Movilidad Internacional Profesores 2022, Banco Santander Chile.

Funding for the Sloan Digital Sky Survey IV has been provided by the Alfred P. Sloan Foundation, the U.S. Department of Energy Office of Science, and the Participating Institutions. SDSS-IV acknowledges support and resources from the Center for High Performance Computing at the University of Utah. The SDSS website is [www.sdss.org](http://www.sdss.org).

SDSS-IV is managed by the Astrophysical Research Consortium for the Participating Institutions of the SDSS Collaboration, including the Brazilian Participation Group, the Carnegie Institution for Science, Carnegie Mellon University, Center for Astrophysics—Harvard & Smithsonian, the Chilean Participation Group, the French Participation Group, Instituto de Astrofísica de Canarias, Johns Hopkins University, Kavli Institute for the Physics and Mathematics of the Universe (IPMU)/University of Tokyo, the Korean Participation Group, Lawrence Berkeley National Laboratory, Leibniz Institut für

Astrophysik Potsdam (AIP), Max-Planck-Institut für Astronomie (MPIA Heidelberg), Max-Planck-Institut für Astrophysik (MPA Garching), Max-Planck-Institut für Extraterrestrische Physik (MPE), National Astronomical Observatories of China, New Mexico State University, New York University, University of Notre Dame, Observatório Nacional/MCTI, The Ohio State University, Pennsylvania State University, Shanghai Astronomical Observatory, United Kingdom Participation Group, Universidad Nacional Autónoma de México, University of Arizona, University of Colorado Boulder, University of Oxford, University of Portsmouth, University of Utah, University of Virginia, University of Washington, University of Wisconsin, Vanderbilt University, and Yale University.

This work has made use of data from the European Space Agency (ESA) mission Gaia (<https://www.cosmos.esa.int/gaia>), processed by the Gaia Data Processing and Analysis Consortium (DPAC, <https://www.cosmos.esa.int/web/gaia/dpac/consortium>). Funding for the DPAC has been provided by national institutions, in particular the institutions participating in the Gaia Multilateral Agreement.

This research has made use of the SIMBAD database, operated at CDS, Strasbourg, France.

*Facilities:* Du Pont (APOGEE), Sloan (APOGEE), 2MASS, Gaia, PanStars1.

*Software:* astropy (Astropy Collaboration et al. 2013, 2018), TopCat (Taylor 2005), R (R Core Team 2018). Additional data analyses were done using IDL version 7.0 (Exelis Visual Information Solutions, Boulder, Colorado).

## Appendix A Target Summary for All Regions

**Table 3**  
Summary of APOGEE-2 Young Cluster Targets

Main Target Region	R.A.	Decl.	Plate ID	MJDs	Subprogram	No. of Targets <sup>a,b</sup>
Single-field Regions						
$\alpha$ Persei	51.62	49.0	9662	57821, 58097, 58148, 58179, 58419, 58446	YSO	255
IC348-RV	55.90	32.00	10100	58058, 58061, 58084, 58085, 58087	YSO, BTX	968
			12706	59063, 59066, 59071, 59072, 59146		
NGC 1333	52.60	31.25	6224	56561	YSO	645
			6225	56236		
			6226	56315		
			7070	56671		
			7071	56674		
			7072	56563, 56607		
NGC 1333-RV			11425	58447, 58527, 58744, 58733, 58775, 58791, 58796, 58803, 58820, 58828, 58831, 58850, 59077	YSO, BTX	264
NGC 2264	100.27	9.68	10302	58061, 58067, 58068, 58086, 58089, 58096	YSO	252
Vela Ridge (265+01-C)	134.43072	-43.54588	12276	58882, 58883	LCO	252
Multiple-field Regions						
<i>California cloud</i>						
California (160-09)	63.06	38.40	11432	58383, 58384	AS4	1763
California (161-06)	65.71	39.93	11433	58443		
California (162-11)	63.39	35.80	11434	58418		
California (163-05)	68.70	38.74	11435	58441		
California (163-08)	66.16	37.25	11436	58444		
California (165-07)	68.80	35.97	11437	58442		

**Table 3**  
(Continued)

Main Target Region	R.A.	Decl.	Plate ID	MJDs	Subprogram	No. of Targets <sup>a</sup> <sub>.b</sub>
California (164-10)	66.38	34.59	11438	58448		
<i>Carina arm</i>						
Carina (160-60-C)	160.86041	-59.62363	11620	58560, 59180	LCO	1406
Carina (161-60-C)	161.15234	-59.82986	11621	58560, 58626		
Carina (162-60-C)	161.63592	-59.83055	11622	58654, 58883		
Carina (287-01-C)	160.54833	-59.5016	12357	58914, 59187		
Carina (288-00-C)	162.4802	-59.54877	12356	58914, 59187, 59223		
Carina (288-01-C-b)	161.00154	-59.87431	9752	59202		
Carina (288-01-C-m)	161.33551	-60.43674	12358	58914		
<i>Cygnus-X complex</i>						
Cygnus-X N	309.25	41.87	11271	58389	BTX	3372
			11272	58390		
			11273	58418		
			11274	58643, 58646		
			11275	58650		
			11276	58653		
Cygnus-X C	306.65	41.01	11409	58625, 58626, 58627	BTX	
			11410	58629		
			11411	58647, 58649		
			11412	58654, 58655		
			11413	58656		
			11414	58659		
Cygnus-X S	305.66	38.57	11415	58637, 58642, 58732	BTX	
			11416	58653		
			11417	58654		
			11418	58656		
			11419	58657, 58658		
			11420	58659		
$\lambda$ Ori						
$\lambda$ Ori B	82.34	11.73	8885	57409	YSO	1742
			8886	57411, 57413		
			8887	57678		
$\lambda$ Ori C	86.6	8.99	9482	57685	YSO	
			9537	58115, 58116		
			9538	58067		
$\lambda$ Ori A	84.14	10.34	8879	57406, 57411	YSO	
			8880	57413, 57648, 57649		
			8881	57650		
			8882	57651, 57655		
			8883	57656, 57675		
			8884	57676, 57677		
<i>Orion AB complex</i>						
Orion A-A	84.1001	-5.1003	9481	58391, 58417, 58420, 58424, 58441	YSO	9538
Orion A-B	83.5496	-5.2996	9533	57737, 57762, 57794, 58085, 58060, 58063		
Orion A-C	84.2507	-6.8994	9659	57790, 57792, 57793		
Orion A-D	84.4999	-7.2005	9660	57790, 57792, 57793		
Orion A-E	85.2001	-8.6996	9661	57795		
Orion B-A	86.654	0.134	8890	57433	YSO	
			8891	57443		
			8892	57675, 57677		
			8893	57677, 57678		
Orion B-B	85.416	-2.12	8894	57433		
			8895	57434		
			8896	57435		
			8897	57436		
			8898	57654		
			8899	57680		
Orion OB1ab-A	84.1	-2.2	9468	57794, 57795	YSO	
			9469	58033, 58037		
			9470	58038		
Orion OB1ab-B	84.0	0.7	9471	57683		
			9472	57684		
			9473	57707		

**Table 3**  
(Continued)

Main Target Region	R.A.	Decl.	Plate ID	MJDs	Subprogram	No. of Targets <sup>a</sup> <sub>.b</sub>
Orion OB1ab-C	82.5	−1.5	9474	57708		
			9475	57732,57734		
			9476	57764		
Orion OB1ab-D	80.7	−1.8	9477	57796		
			9478	57708		
			9479	57713		
Orion OB1ab-E	81.5	1.0	9480	58384		
			8900	57648		
			8901	57649, 57650		
			8902	57652, 57653		
Orion OB1ab-F	82.0	3.0	8903	57675		
			8904	57676		
			8905	57410		
			8906	57411, 57412		
Orion Nebula Cluster (209-20-C)	83.71766	−5.55237	12273	58882,58883	LCO	(278)
Orion A-RV	83.5	−5.4	11593	58477, 58496, 58500, 58532, 58767, 58769 58772, 58775, 58778, 58797, 58802, 58805	BTX	(263)
Orion B-RV	84.4	−7.1	11594	58497, 58501, 58504, 58773, 58779, 58801, 58804 58822, 58828, 58831, 58835, 58850, 58853, 58861	BTX	(265)
<i>Pleiades Cluster</i>						
Pleiades	56.712917	24.175889	5534	55847, 55851, 55854	Core Survey	786
Pleiades-E	57.5	24.1	8888	57408, 57469, 57652	YSO	(523)
Pleiades-W	55.45	24.7	9257	57684, 57764, 58037		
<i>Rosette complex</i>						
Rosette (206-02)	98.20038	4.27645	11440	58474	LCO	1031
			11441	58474, 59201, 59224		
Rosette	98.01	4.8	12266	58828,58829,58830,58831,58834,58857,58860	YSO,BTX	
<i>Taurus-Auriga complex</i>						
Taurus L1495	64.75	27.65	9258	57682, 58007, 58009, 58010, 58036, 58039	YSO	2833
Taurus L1495	64.5	29.2	11592	58499, 58503, 58744, 58854	YSO, BTX	
Taurus L1517	74.0	30.75	11426	58414, 58417	YSO,BTX	
			11426	58417		
			11427	58438, 58439		
			11428	58444		
Taurus L1521	67.0	25.9	9287	57710, 57737, 57761	YSO	
Taurus L1527	69.45	24.75	9288	57711, 57738, 57765		
Taurus L1536	68.48	23.65	9259	57683, 57712, 58010		
Taurus L1551	68.25	18.125	11429	58385	YSO, BTX	
			11430	58386		
			11431	58392,58421		
<i>W3/W4/W5 complex</i>						
W3/W4	37.1726	61.4056	9245	57710, 57764	ASP	1802
			9246	57650		
			9247	57677		
			9248	57762		
			9249	57766, 58008		
			9250	58037		
W3/W4 (btx)	37.17	61.4	11600	58467	YSO, BTX	
			11601	58501		
			11602	58733, 58738		
W5	43.37	60.8982	9251	58007	ASP	(1061)
W5			9252	58008		
W5			9253	58009		
W5			9255	58029		
W5			9256	58039		
W5-a	43.5	60.65	9542	57733	ASP	
Auxiliary Fields						
Carina (285+00)	157.78603	−58.04926	10174	58114, 58117, 58145	Core Survey	(261)
Cygnus-X (075+00)	305.22904	36.605611	5525	56466, 56472, 56541, 56560	Core Survey	(259)
Cygnus-X (079+00)	308.1882	39.8618	7534	56934, 56937, 56962	Core Survey	(390)
			7789	57297, 57579, 57643		

**Table 3**  
(Continued)

Main Target Region	R.A.	Decl.	Plate ID	MJDs	Subprogram	No. of Targets <sup>a</sup> <sub>.b</sub>
Cygnus-X (083+00)	311.0139	42.6438	6082	56231, 56439, 56440, 56449	Core Survey	(263)
Pleiades (169-24)	58.161499	22.248699	10362	58121, 58146, 58151, 58386	BTX	(462)
	58.1615	22.2487	11220	58441, 58447, 58477		
Pleiades (167-24)	56.3324	23.6689	12129	58777, 58881	BTX	(264)

**Note.**

<sup>a</sup> We list the total number of unique targets in the first entry of each region. For some regions the counts for specific subprograms are indicated in parentheses.

**Appendix B****APOGEE-2 Subprograms Relevant to This Study**

1. *Goal Science Program* (YSO): APOGEE-2 Goal Science Programs were defined to fill spaces in the LST distribution after scheduling of the core program, without driving survey requirements. Several young stellar clusters were targeted to characterize embedded populations. These included an extension of the SDSS-III IN-SYNC program (Cottaar et al. 2014).
2. *Ancillary Science Program* (ASP): two calls for ancillary science projects were made during the 5 yr span of the main survey, assigning time to 23 projects, among which was the pilot survey of the W3/W4/W5 complex, aimed at investigating the massive star-forming region.
3. *Bright Time Extension Program* (BTX): This program was a 1.5 yr extension to the main survey that resulted from an unexpected bright time observing efficiency gain. Several additional star-forming regions were proposed in this program.
4. *After Sloan IV Program* (AS4): As part of the BTX, a number of fields were assigned to science projects aimed at enabling the transition toward the SDSS-V survey. The survey of the California complex is in this category.
5. *APOGEE-2S Chilean Time Allocation* (LOC): A number of contributed<sup>27</sup> programs were proposed by Chilean scientists through the Chilean National Time Allocation Committee (CNTAC) or through the TAC of the Carnegie Institution for Science (CIS). Several star-forming regions in the southern sky were observed through these programs.

**Appendix C****Program Description and Selection of Individual Regions**

*$\alpha$  Persei Cluster.*—The  $\alpha$  Persei Cluster was proposed for the YSO program among a list of flagship clusters containing young stars in low-extinction environments. This nearby stellar group with a significant content of intermediate-mass stars and with an spectroscopic age of about 50 Myr (Basri & Martín 1999) provides a good comparison field for the Pleiades and other young, no longer embedded populations.

*California cloud.*—The seven-field survey of the California molecular cloud for the AS4 subprogram includes observations of a sample of embedded stars in the young cluster LKH $\alpha$ -101

but also a significant number of solar-type (G, F) targets selected to be at the expected distance of the cloud (about 400 pc; see Lada et al. 2009), to compare the kinematics of the local population with that of the molecular cloud gas.

*Carina arm.*—The Carina arm data presented in this paper are composed of observations proposed by several authors, mostly through CNTAC/CIS assignments for researchers based in Chilean universities: (a) Programs 283-01-C, 290-01-C and 291-00-C were proposed as a survey of massive stars toward the young complexes Westerlund 2, NGC 3496, NGC 3576, and NGC 3603 in the Carina arm, including surrounding regions, as described in Roman-Lopes et al. (2020b). (b) Fields 287-01-C, 288-01-C, 288-00-C, and 288-01-C, along with fields 160-60-C, 160-61-C, and 162-60-C, constitute two proposals with the common goal of exploring the kinematics of the young population in the NGC 3372 complex at the Carina molecular cloud and comparing the physical and dynamical properties of the young population with those of other regions like Orion.

*Cygnus-X complex.*—The three main regions proposed for the Cygnus-X region as part of the BTX extension of the young star program aim to study the population of the Cygnus OB2 association, targets in the embedded cluster population at the north and south portions of the Cygnus-X molecular complex, and candidate YSO to intermediate-mass and massive stars toward the southern M29/Cygnus OB1/OB9 regions.

*IC 348 and NGC 1333 clusters.*—These data sets had the main goal to reinforce the SDSS-III IN-SYNC samples obtained for the embedded clusters IC 348 and NGC 1333 in the Perseus molecular cloud (Cottaar et al. 2015; Yao et al. 2018). Targets were selected in order to obtain precise radial velocities to explore the presence of spectroscopic binaries. Visits were divided among the YSO and the BTX programs, with the second group being specifically designed to measure RV variations aimed at finding spectroscopic binaries.

*NGC 2264.*—The NGC 2264 cluster in Monoceros was also studied as part of the IN-SYNC survey during SDSS-III, with the main goal of characterizing spectroscopic binaries through RV analysis. Partial results that combine targets in NGC 2264, the two Perseus clusters, and Orion A were published by Fernandez et al. (2017). The YSO and BTX program for NGC 2264 in APOGEE-2 was aimed at exploring the properties of young stars and expanding the study of spectroscopic binaries in the embedded population.

*Orion complex.*—We are including a new data set for the Orion complex survey as part of the uniform exploration of the stellar parameters for young stars across the DR16 and DR17 data sets. A detailed description of the Orion complex survey using data from the main APOGEE-2 YSO goal science

<sup>27</sup> “Contributed” in this case means that the data obtained for such programs end up forming part of the main survey after proprietary time. This is in contrast with the so-called “External” programs, which would remain proprietary to the principal investigators after the end of the survey.

program can already be found in Cottle et al. (2018) and Kounkel et al. (2018). In this paper, we are also including targets from the program 209-20-C, which had as its main goal to study the kinematics of members in and around the ONC to test cluster formation scenarios, particularly how they relate to the integral-shaped filament that runs across the region (Stutz & Gould 2016; Stutz 2018).

Orion is a very extended region with a complex morphology and kinematics and contains groups that vary in evolutionary state from deeply embedded to fully exposed. We made a simple separation of the survey into four subregions: Orion A, covering the ONC and the active molecular complex to the south; Orion B, covering the embedded clusters NGC 2071 and NGC 2024 in the northern filament, as well as the cluster  $\sigma$  Ori, which expands from the southernmost tip west of the Horsehead Nebula; Orion OB1, encompassing all the APOGEE-2 fields to the northwest of  $\sigma$  Ori; and  $\lambda$  Ori, which spans three fields covering the Collinder 69 cluster and the flanking groups B30 and B35, expanding along with a large molecular ring (e.g., Dolan & Mathieu 2001, 2002).

In order to make this division, the fields labeled as ORIONA, ORIONC,D,E, and ONCB were assigned to Orion A. The fields labeled as ORIONB (minus those corresponding to ONC) and those belonging to fields ORIONOB1A-A located east and south of  $(\alpha, \delta) = (83.94, -0.96)$  were assigned to Orion B. The rest of the fields, labeled as ORIONOB1, were assigned to the region Orion OB1 (see Table 3 for details).

*Pleiades Cluster.*—The Pleiades Cluster is a prototypical young open cluster located at a nearby distance of 134 pc (e.g., Percival et al. 2005). It stands as a very important calibrator for the determination of the spectral parameters of young stars (SDSS-III IN-SYNC; Cottaar et al. 2014), and its study is capital for the understanding of how young clusters in the solar neighborhood evolve, expand, and eventually integrate into the disk population. The Pleiades fields proposed in the YSO program aim to expand the pilot set explored in SDSS-III, eventually contributing to a robust collection of Pleiades members with precise spectral characterization.

*Rosette complex.*—The Rosette was proposed as a BTX target for the YSO program by teams in both hemispheres. A first proposal for LCO aimed at obtaining, for the first time, a significantly large sample of embedded star targets in the Rosette molecular cloud, and comparing against targets in the NGC 2244 OB association at the Rosette Nebula. The other team also proposed to observe a sample combining embedded and emerged targets in the cluster population. In the end, scientific targets were merged for a joint project with six visits using BTX time, using as common goals to trace the young star population and to explore the evolution of the family of young clusters across the complex.

*Taurus-Auriga complex.*—This region, one of the closest low-mass star formation complexes, has been the target of numerous spectroscopic studies in the past. The main goals are to characterize the properties, evolution, and kinematics of

groups of young low-mass stars across the filamentary structure of the Taurus molecular cloud. A first approach to the 6D distribution of the young star groups in Taurus combining precise parallax information from both Gaia DR2 and VLA observations, along with radial velocity information from APOGEE Net (Olney et al. 2020), can be found in Galli et al. (2019). This and subsequent studies aim for the characterization of the young stellar population using APOGEE-2 data.

*Vela C cloud.*—One APOGEE field was dedicated to exploring the Vela C molecular cloud complex, encompassing the RCW34 and RCW36 (Gum19 and Gum20) active star-forming regions. The Vela C complex is an interesting region that combines both low-mass and massive star formation (Massi et al. 2019), and the APOGEE observations aim at similar goals to those in Carina, Cygnus-X, and W3/W4/W5: the exploration of young cluster sources in the presence of massive members.

*W3/W4/W5 complex.*—An APOGEE-2 survey of the W3, W4, and W5 massive star-forming regions in the Perseus arm was proposed as an ASP program with two main goals: The first goal was to test APOGEE for the study of hot, massive sources. Until then, a small number of blue sources were added to each core survey plate for the purposes of removing telluric atmospheric lines during the reduction process (Nidever et al. 2015), but it was not clear whether the scarcity of features in the *H*-band spectral window was enough to provide a reliable spectral classification for O and B sources. This way a list of 240 targets containing both confirmed types and photometric candidates was provided, resulting in a successful methodology for the identification and classification of O and B stars down to one spectral subtype (Roman-Lopes et al. 2018; Ramírez-Preciado et al. 2020), which appears to extend nicely to A stars (V. Ramírez-Preciado 2022, in preparation) and represents to date the most reliable classification of intermediate- to high-mass stars in the absence of a set of synthetic atmosphere models adequate for the APOGEE near-IR spectral range. The second goal was to study the young stellar population in the FGK-type regime in a massive star-forming region like W3/W4/W5, to investigate the limitations of our methodologies in the presence of high extinction and less reliable parallax data. Two APOGEE fields were used for this program, covering nicely the areas of the W3/W4 and W5 regions, respectively. Two small extensions to add visits to these fields were added during the second ancillary call and the BTX programs.

## Appendix D Stellar Properties

This version of the manuscript shows an abridged version of Table 4, containing the first 10 entries of each region in the catalog, in order to facilitate commenting and edition of the manuscript. It is expected that the electronic version of the paper would contain a full version of the table in electronic format.

**Table 4**  
Probable Region Members

APOGEE-ID	R.A. J2000	Decl.	$A_V$ (mag)	$r_{\text{geo}}$ (pc)	$T_{\text{eff}}$ (K)	$\log g$	[Fe/H]	$\log L/L_{\odot}$	$M/M_{\odot}$	Age (Myr)
$\alpha$ Persei Cluster										
2M03190241+4933375	49.759998	49.560398	$0.7^{+0.13}_{-0.11}$	$175.37^{+0.81}_{-0.55}$	$3.60 \pm 0.006$	$4.29 \pm 0.030$	$-0.09 \pm 0.019$	$-1.07 \pm 0.020$	$0.6^{+0.01}_{-0.00}$	$87.4^{+6.25}_{-7.32}$
2M03192494+4859402	49.853901	48.994499	$0.1^{+0.07}_{-0.05}$	$164.89^{+2.16}_{-2.27}$	$3.51 \pm 0.003$	$4.63 \pm 0.052$	$0.04 \pm 0.010$	$-1.72 \pm 0.030$	$0.4^{+0.01}_{-0.01}$	$82.4^{+5.44}_{-3.92}$
2M03193117+4941171	49.879902	49.688099	$0.8^{+0.23}_{-0.24}$	$176.31^{+1.90}_{-1.90}$	$3.53 \pm 0.011$	$4.26 \pm 0.086$	$-0.08 \pm 0.036$	$-1.59 \pm 0.027$	$0.4^{+0.01}_{-0.03}$	$140.1^{+90.49}_{-39.12}$
2M03195729+4904215	49.988701	49.072701	$0.1^{+0.04}_{-0.04}$	$163.91^{+0.98}_{-1.10}$	$3.54 \pm 0.001$	$4.74 \pm 0.021$	$0.04 \pm 0.006$	$-1.37 \pm 0.014$	$0.5^{+0.00}_{-0.00}$	$60.7^{+3.91}_{-3.63}$
2M03201212+4856412	50.050499	48.944801	$0.1^{+0.05}_{-0.07}$	$169.36^{+1.11}_{-0.94}$	$3.53 \pm 0.002$	$4.76 \pm 0.028$	$0.06 \pm 0.009$	$-1.38 \pm 0.020$	$0.5^{+0.01}_{-0.01}$	$47.7^{+2.75}_{-2.38}$
2M03204185+4824375	50.174400	48.410400	$0.1^{+0.05}_{-0.04}$	$169.20^{+0.57}_{-0.54}$	$3.71 \pm 0.001$	$4.50 \pm 0.009$	...	$-0.41 \pm 0.014$	$0.8^{+0.01}_{-0.01}$	$40.0^{+2.42}_{-1.07}$
2M03205158+4927574	50.214901	49.466000	$0.2^{+0.04}_{-0.03}$	$172.75^{+0.32}_{-0.35}$	$3.67 \pm 0.001$	$4.39 \pm 0.013$	...	$-0.57 \pm 0.013$	$0.8^{+0.01}_{-0.01}$	$36.1^{+1.99}_{-1.74}$
2M03210651+4826127	50.277100	48.436901	$0.2^{+0.04}_{-0.04}$	$171.98^{+0.30}_{-0.34}$	$3.68 \pm 0.001$	$4.59 \pm 0.011$	...	$-0.60 \pm 0.013$	$0.8^{+0.01}_{-0.01}$	$47.7^{+3.69}_{-2.19}$
2M03212020+4845270	50.334202	48.757500	$0.2^{+0.04}_{-0.05}$	$172.87^{+0.42}_{-0.44}$	$3.71 \pm 0.001$	$4.52 \pm 0.009$	...	$-0.37 \pm 0.012$	$0.8^{+0.01}_{-0.00}$	$39.8^{+1.85}_{-1.44}$
2M03212047+4753152	50.335300	47.887600	$1.1^{+0.25}_{-0.29}$	$170.03^{+0.83}_{-0.87}$	$3.60 \pm 0.012$	$4.21 \pm 0.031$	...	$-1.11 \pm 0.030$	$0.6^{+0.01}_{-0.02}$	$121.7^{+7.31}_{-11.29}$
California Cloud										
2M04212799+3345498	65.366699	33.763901	$0.6^{+0.06}_{-0.05}$	$496.91^{+4.73}_{-4.92}$	$3.71 \pm 0.004$	$4.43 \pm 0.037$	...	$-0.05 \pm 0.023$	$1.1^{+0.02}_{-0.01}$	$14.9^{+0.80}_{-0.83}$
2M04222320+3820491	65.596703	38.347000	$2.3^{+0.09}_{-0.06}$	$522.27^{+6.99}_{-8.13}$	$3.67 \pm 0.004$	$4.34 \pm 0.061$	...	$0.24 \pm 0.022$	$1.2^{+0.09}_{-0.05}$	$2.0^{+0.25}_{-0.20}$
2M04232189+3352172	65.841202	33.871498	$0.5^{+0.23}_{-0.23}$	$525.67^{+4.66}_{-5.10}$	$3.73 \pm 0.017$	$3.75 \pm 0.232$	...	$0.22 \pm 0.060$	$1.3^{+0.02}_{-0.02}$	$9.2^{+1.96}_{-1.37}$
2M04254131+3537189	66.422096	35.621899	$1.5^{+0.06}_{-0.05}$	$538.79^{+4.95}_{-4.43}$	$3.73 \pm 0.003$	$4.22 \pm 0.028$	...	$0.59 \pm 0.018$	$1.8^{+0.02}_{-0.02}$	$3.6^{+0.21}_{-0.24}$
2M04254864+3900413	66.452698	39.011501	$1.0^{+0.24}_{-0.33}$	$513.42^{+4.52}_{-3.89}$	$3.74 \pm 0.020$	$3.34 \pm 0.266$	...	$0.27 \pm 0.070$	$1.3^{+0.03}_{-0.04}$	$9.6^{+2.46}_{-2.30}$
2M04260844+3335174	66.535202	33.588200	$0.9^{+0.03}_{-0.04}$	$533.22^{+5.28}_{-3.51}$	$3.71 \pm 0.002$	$3.92 \pm 0.042$	...	$0.55 \pm 0.014$	$1.8^{+0.02}_{-0.02}$	$2.2^{+0.10}_{-0.09}$
2M04271110+3521514	66.796303	35.364300	$1.6^{+0.05}_{-0.04}$	$539.05^{+6.09}_{-10.10}$	$3.68 \pm 0.002$	$4.30 \pm 0.034$	...	$0.20 \pm 0.018$	$1.3^{+0.02}_{-0.02}$	$3.3^{+0.24}_{-0.20}$
2M04275080+3631263	66.961700	36.523998	$4.5^{+0.39}_{-0.37}$	$535.75^{+81.01}_{-37.69}$	$3.57 \pm 0.012$	$3.98 \pm 0.134$	$-0.11 \pm 0.066$	$-0.56 \pm 0.140$	$0.6^{+0.07}_{-0.09}$	$4.3^{+2.99}_{-2.40}$
2M04291155+3504495	67.298103	35.080399	$1.6^{+0.07}_{-0.07}$	$528.00^{+19.11}_{-12.11}$	$3.58 \pm 0.003$	$4.17 \pm 0.048$	$-0.01 \pm 0.013$	$-0.30 \pm 0.027$	$0.6^{+0.01}_{-0.02}$	$2.0^{+0.23}_{-0.19}$
2M04291206+3734394	67.300301	37.577599	$1.8^{+0.11}_{-0.08}$	$515.17^{+5.02}_{-4.95}$	$3.73 \pm 0.008$	$3.85 \pm 0.084$	...	$0.38 \pm 0.033$	$1.5^{+0.03}_{-0.02}$	$6.4^{+0.64}_{-0.65}$
Carina Complex										
2M10442327-5928115	161.097000	-59.469898	$1.5^{+0.08}_{-0.09}$	$2415.07^{+295.17}_{-261.81}$	$3.68 \pm 0.011$	$3.73 \pm 0.239$	...	$0.50 \pm 0.104$	$1.3^{+0.20}_{-0.15}$	$1.1^{+0.49}_{-0.38}$
2M10445950-5926040	161.248001	-59.434498	$2.6^{+0.19}_{-0.16}$	$2619.04^{+532.31}_{-347.70}$	$3.69 \pm 0.018$	$3.87 \pm 0.247$	...	$1.08 \pm 0.151$	$1.7^{+0.52}_{-0.43}$	...
2M10431426-5912128	160.809402	-59.203602	$1.2^{+0.13}_{-0.10}$	$2351.07^{+224.81}_{-206.38}$	$3.69 \pm 0.012$	$3.71 \pm 0.242$	...	$0.63 \pm 0.083$	$1.6^{+0.19}_{-0.20}$	$1.1^{+0.41}_{-0.26}$
2M10431400-5923538	160.808395	-59.398300	$1.6^{+0.07}_{-0.08}$	$2925.19^{+496.76}_{-334.78}$	$3.69 \pm 0.007$	$4.16 \pm 0.087$	...	$0.76 \pm 0.111$	$1.6^{+0.19}_{-0.15}$	$0.7^{+0.26}_{-0.24}$
2M10444199-6007385	161.175003	-60.127399	$1.0^{+0.22}_{-0.17}$	$2154.54^{+145.01}_{-125.79}$	$3.69 \pm 0.022$	$4.11 \pm 0.137$	...	$0.71 \pm 0.072$	$1.6^{+0.40}_{-0.35}$	$0.8^{+0.53}_{-0.32}$
2M10441794-5929263	161.074799	-59.490601	$1.5^{+0.10}_{-0.09}$	$2494.46^{+230.46}_{-163.00}$	$3.71 \pm 0.011$	$3.52 \pm 0.275$	...	$0.99 \pm 0.081$	$2.3^{+0.28}_{-0.26}$	$0.8^{+0.19}_{-0.16}$
2M10421485-5923140	160.561905	-59.387199	$3.2^{+0.21}_{-0.15}$	$2658.67^{+290.96}_{-283.10}$	$3.71 \pm 0.018$	$4.20 \pm 0.093$	...	$1.47 \pm 0.103$	$3.2^{+0.39}_{-0.74}$	...
2M10451232-5949490	161.301300	-59.830299	$4.6^{+0.28}_{-0.24}$	$2370.16^{+947.61}_{-699.37}$	$3.72 \pm 0.014$	$4.25 \pm 0.118$	...	$0.64 \pm 0.263$	$1.9^{+0.45}_{-0.32}$	$2.4^{+2.11}_{-1.32}$
2M10440449-5958274	161.018707	-59.974300	$1.6^{+0.12}_{-0.13}$	$2226.21^{+179.77}_{-153.00}$	$3.72 \pm 0.013$	$3.52 \pm 0.248$	...	$0.79 \pm 0.071$	$2.1^{+0.12}_{-0.13}$	$1.8^{+0.63}_{-0.54}$
2M10443931-5923550	161.163803	-59.398602	$0.0^{+0.00}_{-0.00}$	$2469.66^{+85.38}_{-68.37}$	$3.72 \pm 0.016$	$3.99 \pm 0.122$	...	$0.88 \pm 0.033$	$2.3^{+0.06}_{-0.11}$	$1.6^{+0.63}_{-0.40}$
Cygnus-X Complex										
2M20261538+3909148	306.564087	39.154099	$4.9^{+0.11}_{-0.13}$	$1911.58^{+442.69}_{-319.51}$	$3.70 \pm 0.012$	$4.28 \pm 0.078$	...	$0.89 \pm 0.157$	$1.7^{+0.30}_{-0.21}$	$0.6^{+0.43}_{-0.19}$
2M20261791+3855247	306.574707	38.923500	$2.7^{+0.10}_{-0.09}$	$1653.57^{+64.02}_{-61.35}$	$3.74 \pm 0.013$	$4.07 \pm 0.087$	...	$0.87 \pm 0.046$	$2.3^{+0.08}_{-0.09}$	$2.0^{+0.41}_{-0.46}$
2M20262157+3957387	306.589905	39.960800	$5.4^{+0.16}_{-0.09}$	$1652.08^{+103.69}_{-101.28}$	$3.78 \pm 0.006$	$4.09 \pm 0.048$	...	$1.49 \pm 0.049$	$2.9^{+0.09}_{-0.09}$	$1.8^{+0.18}_{-0.15}$
2M20262249+3848142	306.593689	38.804001	$2.6^{+0.15}_{-0.30}$	$1650.49^{+39.02}_{-36.82}$	$3.80 \pm 0.021$	$4.42 \pm 0.061$	...	$1.51 \pm 0.063$	$2.7^{+0.06}_{-0.08}$	$2.2^{+0.27}_{-0.29}$
2M20262334+4047281	306.597290	40.791199	$3.6^{+0.17}_{-0.19}$	$1660.74^{+138.13}_{-119.48}$	$3.71 \pm 0.019$	$4.32 \pm 0.064$	...	$0.71 \pm 0.082$	$2.0^{+0.15}_{-0.23}$	$1.9^{+0.71}_{-0.60}$

**Table 4**  
(Continued)

APOGEE-ID	R.A. J2000	Decl.	$A_V$ (mag)	$r_{\text{geo}}$ (pc)	$T_{\text{eff}}$ (K)	log g	[Fe/H]	log $L/L_{\odot}$	$M/M_{\odot}$	Age (Myr)
2M20262833+4104084	306.618103	41.069000	$3.2^{+0.21}_{-0.19}$	$1738.39^{+155.15}_{-106.80}$	$3.69 \pm 0.020$	$3.98 \pm 0.150$	...	$0.76 \pm 0.084$	$1.5^{+0.35}_{-0.42}$	$0.6^{+0.28}_{-0.26}$
2M20263035+4009464	306.626495	40.162899	$4.7^{+0.18}_{-0.17}$	$1490.33^{+157.92}_{-123.91}$	$3.70 \pm 0.016$	$4.19 \pm 0.129$	...	$1.07 \pm 0.087$	$2.0^{+0.53}_{-0.42}$	...
2M20263850+3933473	306.660400	39.563099	$4.1^{+0.08}_{-0.07}$	$1712.00^{+105.40}_{-105.44}$	$3.80 \pm 0.011$	$4.05 \pm 0.083$	...	$1.06 \pm 0.055$	$1.9^{+0.07}_{-0.08}$	$5.7^{+0.62}_{-0.62}$
2M20264171+3837422	306.673798	38.628399	$4.0^{+0.10}_{-0.22}$	$1616.41^{+59.67}_{-47.99}$	$3.83 \pm 0.021$	$4.23 \pm 0.075$	...	$1.60 \pm 0.071$	$2.7^{+0.07}_{-0.08}$	...
2M20265498+3937459	306.729095	39.629398	$4.0^{+0.13}_{-0.43}$	$1721.35^{+62.54}_{-73.27}$	$3.79 \pm 0.020$	$4.32 \pm 0.095$	...	$1.59 \pm 0.086$	$3.0^{+0.12}_{-0.07}$	$1.7^{+0.19}_{-0.26}$
IC 348										
2M03441361+3215542	56.056702	32.265099	$4.5^{+0.17}_{-0.14}$	$330.33^{+19.47}_{-20.74}$	$3.56 \pm 0.001$	$3.79 \pm 0.035$	$0.02 \pm 0.005$	$-0.56 \pm 0.060$	$0.6^{+0.03}_{-0.03}$	$3.8^{+1.31}_{-1.03}$
2M03441642+3209552	56.068401	32.165401	$1.2^{+0.03}_{-0.04}$	$311.22^{+3.01}_{-3.85}$	$3.65 \pm 0.001$	$4.13 \pm 0.018$	...	$-0.13 \pm 0.016$	$1.0^{+0.01}_{-0.01}$	$4.6^{+0.28}_{-0.30}$
2M03441816+3204570	56.075699	32.082500	$6.9^{+0.11}_{-0.08}$	$326.02^{+13.91}_{-16.59}$	$3.69 \pm 0.002$	$4.29 \pm 0.021$	...	$0.31 \pm 0.043$	$1.5^{+0.04}_{-0.03}$	$2.9^{+0.60}_{-0.32}$
2M03441857+3212530	56.077400	32.214699	$5.4^{+0.26}_{-0.26}$	$293.19^{+29.66}_{-25.74}$	$3.62 \pm 0.020$	$4.08 \pm 0.139$	...	$-0.67 \pm 0.084$	$0.8^{+0.05}_{-0.02}$	$20.4^{+8.92}_{-7.43}$
2M03442129+3211563	56.088699	32.199001	$2.2^{+0.04}_{-0.06}$	$314.77^{+9.04}_{-7.11}$	$3.56 \pm 0.001$	$4.03 \pm 0.033$	$0.04 \pm 0.005$	$-0.65 \pm 0.025$	$0.6^{+0.01}_{-0.01}$	$5.8^{+0.85}_{-0.61}$
2M03442155+3210174	56.089802	32.171501	$2.0^{+0.07}_{-0.06}$	$319.95^{+11.80}_{-7.94}$	$3.56 \pm 0.002$	$3.72 \pm 0.044$	$-0.01 \pm 0.007$	$-0.65 \pm 0.028$	$0.6^{+0.01}_{-0.01}$	$5.4^{+0.70}_{-0.73}$
2M03442161+3210376	56.090099	32.177101	$3.1^{+0.07}_{-0.07}$	$321.73^{+8.40}_{-9.89}$	$3.57 \pm 0.001$	$3.96 \pm 0.037$	$-0.05 \pm 0.008$	$-0.43 \pm 0.029$	$0.6^{+0.02}_{-0.02}$	$2.9^{+0.46}_{-0.37}$
2M03442166+3206248	56.090302	32.106899	$2.0^{+0.07}_{-0.05}$	$315.11^{+7.67}_{-7.00}$	$3.56 \pm 0.001$	$3.95 \pm 0.033$	$0.03 \pm 0.007$	$-0.62 \pm 0.025$	$0.6^{+0.01}_{-0.01}$	$4.8^{+0.53}_{-0.52}$
2M03442228+3205427	56.092899	32.095200	$3.3^{+0.07}_{-0.06}$	$305.26^{+10.90}_{-10.72}$	$3.59 \pm 0.003$	$3.80 \pm 0.077$	$-0.05 \pm 0.009$	$-0.43 \pm 0.033$	$0.7^{+0.00}_{-0.01}$	$4.0^{+0.52}_{-0.45}$
2M03442398+3211000	56.099998	32.183300	$2.1^{+0.04}_{-0.03}$	$315.29^{+2.12}_{-2.21}$	$3.76 \pm 0.002$	$4.22 \pm 0.020$	...	$0.42 \pm 0.013$	$1.4^{+0.01}_{-0.02}$	...
NGC 1333										
2M03280010+3008469	52.000401	30.146400	$3.0^{+0.06}_{-0.06}$	$268.30^{+7.51}_{-5.87}$	$3.53 \pm 0.001$	$3.79 \pm 0.006$	$-0.07 \pm 0.002$	$-0.55 \pm 0.023$	$0.4^{+0.01}_{-0.01}$	$1.7^{+0.22}_{-0.17}$
2M03283173+3059158	52.132198	30.987700	$6.6^{+0.10}_{-0.14}$	$290.35^{+10.94}_{-12.73}$	$3.65 \pm 0.006$	$4.06 \pm 0.043$	...	$0.09 \pm 0.041$	$0.9^{+0.07}_{-0.07}$	$1.7^{+0.30}_{-0.25}$
2M03285101+3118184	52.212601	31.305099	$2.4^{+0.12}_{-0.11}$	$303.16^{+4.43}_{-5.27}$	$3.55 \pm 0.001$	$3.92 \pm 0.023$	$-0.13 \pm 0.005$	$-0.19 \pm 0.022$	$0.3^{+0.01}_{-0.01}$	$0.6^{+0.04}_{-0.07}$
2M03285105+3116324	52.212700	31.275700	$2.6^{+0.24}_{-0.28}$	$282.88^{+8.94}_{-7.70}$	$3.55 \pm 0.009$	$3.78 \pm 0.129$	$-0.04 \pm 0.028$	$-0.99 \pm 0.073$	$0.6^{+0.03}_{-0.05}$	$21.0^{+2.65}_{-2.27}$
2M03285119+3119548	52.213299	31.331900	$3.5^{+0.05}_{-0.03}$	$295.54^{+3.77}_{-3.52}$	$3.61 \pm 0.000$	$3.78 \pm 0.010$	...	$-0.08 \pm 0.015$	$0.7^{+0.00}_{-0.00}$	$1.5^{+0.08}_{-0.08}$
2M03285213+3115471	52.217201	31.263100	$3.8^{+0.20}_{-0.23}$	$298.97^{+10.40}_{-11.92}$	$3.57 \pm 0.013$	$3.37 \pm 0.106$	$-0.26 \pm 0.063$	$-0.68 \pm 0.055$	$0.7^{+0.01}_{-0.04}$	$7.9^{+1.25}_{-0.97}$
2M03285216+3122453	52.217300	31.379299	$1.8^{+0.05}_{-0.04}$	$286.53^{+3.23}_{-4.04}$	$3.56 \pm 0.000$	$3.66 \pm 0.013$	$-0.01 \pm 0.003$	$-0.52 \pm 0.018$	$0.6^{+0.01}_{-0.01}$	$2.9^{+0.26}_{-0.28}$
2M03285461+3116512	52.227501	31.280899	$4.7^{+0.14}_{-0.17}$	$311.51^{+11.23}_{-10.78}$	$3.56 \pm 0.002$	$3.66 \pm 0.043$	$-0.03 \pm 0.007$	$-0.45 \pm 0.036$	$0.5^{+0.02}_{-0.02}$	$2.3^{+0.40}_{-0.34}$
2M03285514+3116247	52.229801	31.273500	$3.4^{+0.19}_{-0.17}$	$290.48^{+10.34}_{-9.86}$	$3.55 \pm 0.005$	$3.96 \pm 0.092$	$0.01 \pm 0.022$	$-0.75 \pm 0.056$	$0.6^{+0.02}_{-0.03}$	$7.0^{+1.74}_{-1.02}$
2M03285622+3117457	52.234299	31.296000	$3.5^{+0.39}_{-0.36}$	$313.03^{+13.24}_{-12.13}$	$3.54 \pm 0.014$	$3.47 \pm 0.195$	$-0.21 \pm 0.068$	$-0.94 \pm 0.117$	$0.6^{+0.06}_{-0.08}$	$12.2^{+2.43}_{-2.32}$
NGC 2264										
2M06390996+1005127	99.791496	10.086900	$1.8^{+0.14}_{-0.13}$	$727.35^{+35.10}_{-33.19}$	$3.56 \pm 0.002$	$4.31 \pm 0.066$	$-0.05 \pm 0.009$	$-0.34 \pm 0.048$	$0.5^{+0.03}_{-0.03}$	$1.5^{+0.37}_{-0.27}$
2M06392200+1006233	99.841698	10.106500	$0.2^{+0.05}_{-0.06}$	$671.48^{+15.13}_{-14.01}$	$3.60 \pm 0.002$	$4.59 \pm 0.020$	$-0.06 \pm 0.010$	$-0.46 \pm 0.024$	$0.7^{+0.00}_{-0.00}$	$4.8^{+0.47}_{-0.40}$
2M06392550+0931394	99.856300	9.527600	$1.3^{+0.10}_{-0.10}$	$656.11^{+31.19}_{-31.26}$	$3.59 \pm 0.004$	$4.46 \pm 0.071$	$-0.08 \pm 0.020$	$-0.49 \pm 0.048$	$0.7^{+0.01}_{-0.01}$	$4.9^{+0.89}_{-0.65}$
2M06393398+0949208	99.891602	9.822500	$0.3^{+0.05}_{-0.04}$	$690.43^{+17.30}_{-14.32}$	$3.59 \pm 0.001$	$4.32 \pm 0.037$	$-0.01 \pm 0.006$	$-0.27 \pm 0.022$	$0.6^{+0.02}_{-0.01}$	$1.9^{+0.22}_{-0.13}$
2M06393931+0955596	99.913803	9.933200	$0.2^{+0.07}_{-0.07}$	$676.12^{+17.63}_{-22.85}$	$3.58 \pm 0.002$	$4.20 \pm 0.038$	$-0.07 \pm 0.009$	$-0.23 \pm 0.030$	$0.6^{+0.02}_{-0.02}$	$1.3^{+0.24}_{-0.13}$
2M06394147+0946196	99.922798	9.772100	$0.3^{+0.05}_{-0.05}$	$710.17^{+12.10}_{-10.31}$	$3.66 \pm 0.002$	$4.40 \pm 0.025$	...	$0.00 \pm 0.021$	$1.1^{+0.02}_{-0.02}$	$4.0^{+0.48}_{-0.41}$
2M06394355+0936039	99.931503	9.601100	$4.4^{+0.11}_{-0.11}$	$674.50^{+76.53}_{-64.17}$	$3.66 \pm 0.002$	$4.47 \pm 0.037$	...	$0.05 \pm 0.079$	$1.0^{+0.03}_{-0.05}$	$2.5^{+0.82}_{-0.81}$
2M06395109+0936328	99.962898	9.609100	$1.1^{+0.14}_{-0.11}$	$711.65^{+44.03}_{-42.72}$	$3.56 \pm 0.005$	$3.98 \pm 0.081$	$-0.06 \pm 0.022$	$-0.62 \pm 0.059$	$0.7^{+0.03}_{-0.03}$	$5.0^{+1.91}_{-1.08}$
2M06395957+0956243	99.998199	9.940100	$0.0^{+0.00}_{-0.00}$	$720.34^{+14.28}_{-14.42}$	$3.60 \pm 0.003$	$4.04 \pm 0.033$	$-0.12 \pm 0.009$	$-0.30 \pm 0.024$	$0.7^{+0.00}_{-0.00}$	$2.6^{+0.22}_{-0.19}$
2M06395984+0933416	99.999397	9.561600	$0.0^{+0.07}_{-0.06}$	$685.16^{+18.91}_{-19.71}$	$3.60 \pm 0.004$	$4.35 \pm 0.081$	$-0.11 \pm 0.016$	$-0.59 \pm 0.029$	$0.7^{+0.00}_{-0.00}$	$8.1^{+1.07}_{-0.81}$

**Table 4**  
(Continued)

APOGEE-ID	R.A. J2000	Decl.	$A_V$ (mag)	$r_{\text{geo}}$ (pc)	$T_{\text{eff}}$ (K)	log g	[Fe/H]	log $L/L_{\odot}$	$M/M_{\odot}$	Age (Myr)
$\lambda$ Ori Complex										
2M05301704+1215410	82.570999	12.261400	$0.5^{+0.05}_{-0.04}$	$399.88^{+5.70}_{-6.75}$	$3.56 \pm 0.001$	$4.04 \pm 0.037$	$0.05 \pm 0.007$	$-0.61 \pm 0.019$	$0.6^{+0.01}_{-0.01}$	$4.5^{+0.48}_{-0.35}$
2M05303607+1206406	82.650299	12.111300	$0.3^{+0.06}_{-0.06}$	$380.25^{+6.36}_{-5.96}$	$3.52 \pm 0.002$	$4.06 \pm 0.032$	$-0.00 \pm 0.007$	$-0.81 \pm 0.021$	$0.4^{+0.01}_{-0.02}$	$3.6^{+0.29}_{-0.42}$
2M05303614+1030543	82.650597	10.515100	$0.3^{+0.05}_{-0.05}$	$390.44^{+2.17}_{-2.31}$	$3.66 \pm 0.002$	$4.21 \pm 0.039$	...	$0.00 \pm 0.018$	$1.1^{+0.01}_{-0.02}$	$3.3^{+0.30}_{-0.27}$
2M05303619+1236524	82.650803	12.614600	$0.8^{+0.08}_{-0.09}$	$385.16^{+3.73}_{-3.54}$	$3.56 \pm 0.003$	$3.78 \pm 0.076$	$-0.03 \pm 0.008$	$-0.17 \pm 0.022$	$0.4^{+0.02}_{-0.01}$	$0.7^{+0.05}_{-0.06}$
2M05303638+1236566	82.651604	12.615700	$0.9^{+0.09}_{-0.08}$	$385.72^{+8.48}_{-7.66}$	$3.53 \pm 0.002$	$3.95 \pm 0.048$	$-0.01 \pm 0.010$	$-0.70 \pm 0.024$	$0.5^{+0.01}_{-0.02}$	$3.3^{+0.37}_{-0.37}$
2M05304096+1244161	82.670700	12.737800	$3.9^{+0.19}_{-0.14}$	$415.80^{+18.94}_{-16.13}$	$3.55 \pm 0.003$	$3.74 \pm 0.056$	$-0.05 \pm 0.009$	$-0.26 \pm 0.045$	$0.4^{+0.02}_{-0.02}$	$0.8^{+0.11}_{-0.09}$
2M05304136+1030325	82.672401	10.509000	$0.3^{+0.08}_{-0.08}$	$396.12^{+2.34}_{-2.43}$	$3.72 \pm 0.006$	$4.03 \pm 0.046$	...	$0.51 \pm 0.025$	$1.8^{+0.04}_{-0.03}$	$3.2^{+0.43}_{-0.39}$
2M05304878+1005218	82.703300	10.089400	$0.6^{+0.09}_{-0.06}$	$391.78^{+5.88}_{-5.54}$	$3.56 \pm 0.002$	$4.17 \pm 0.054$	$0.01 \pm 0.009$	$-0.61 \pm 0.022$	$0.7^{+0.02}_{-0.01}$	$5.5^{+0.57}_{-0.53}$
2M05305801+1001153	82.741699	10.020900	$0.6^{+0.04}_{-0.08}$	$400.45^{+4.74}_{-5.44}$	$3.56 \pm 0.002$	$3.96 \pm 0.071$	$0.02 \pm 0.009$	$-0.58 \pm 0.017$	$0.6^{+0.01}_{-0.01}$	$3.7^{+0.39}_{-0.26}$
2M05310101+1204142	82.754204	12.070600	$0.7^{+0.07}_{-0.09}$	$383.79^{+4.38}_{-5.04}$	$3.56 \pm 0.003$	$3.88 \pm 0.053$	$-0.02 \pm 0.007$	$-0.65 \pm 0.019$	$0.6^{+0.02}_{-0.01}$	$5.4^{+0.56}_{-0.40}$
Orion A Complex										
2M05324266-0459313	83.177803	-4.992000	$0.2^{+0.15}_{-0.10}$	$372.21^{+3.22}_{-2.71}$	$3.57 \pm 0.005$	$4.01 \pm 0.067$	$0.01 \pm 0.014$	$-0.42 \pm 0.028$	$2.3^{+1.71}_{-1.76}$	$2.3^{+0.25}_{-0.20}$
2M05324731-0539426	83.197098	-5.661900	$0.7^{+0.04}_{-0.06}$	$372.94^{+3.39}_{-3.32}$	$3.55 \pm 0.001$	$4.07 \pm 0.030$	$0.06 \pm 0.006$	$-0.53 \pm 0.015$	$2.6^{+2.07}_{-2.09}$	$2.6^{+0.16}_{-0.20}$
2M05325352-0606011	83.223000	-6.100300	$0.8^{+0.13}_{-0.10}$	$372.94^{+8.01}_{-7.03}$	$3.53 \pm 0.003$	$4.15 \pm 0.097$	$0.03 \pm 0.015$	$-0.86 \pm 0.027$	$6.0^{+5.53}_{-5.57}$	$6.0^{+0.88}_{-0.59}$
2M05325531-0412390	83.230499	-4.210800	$0.4^{+0.05}_{-0.04}$	$356.97^{+2.91}_{-3.24}$	$3.57 \pm 0.001$	$4.28 \pm 0.039$	$-0.02 \pm 0.006$	$-0.53 \pm 0.017$	$4.9^{+4.17}_{-4.19}$	$4.9^{+0.45}_{-0.29}$
2M05325630-0603189	83.234596	-6.055300	$0.7^{+0.08}_{-0.14}$	$348.48^{+5.58}_{-4.57}$	$3.56 \pm 0.004$	$4.04 \pm 0.077$	$-0.01 \pm 0.010$	$-0.84 \pm 0.023$	$14.7^{+14.01}_{-14.02}$	$14.7^{+1.75}_{-1.41}$
2M05325690-0512476	83.237099	-5.213200	$1.2^{+0.07}_{-0.07}$	$393.12^{+4.94}_{-4.90}$	$3.57 \pm 0.001$	$4.24 \pm 0.030$	$0.01 \pm 0.003$	$-0.50 \pm 0.018$	$3.2^{+2.62}_{-2.64}$	$3.2^{+0.24}_{-0.26}$
2M05325791-0602429	83.241302	-6.045300	$0.6^{+0.11}_{-0.12}$	$380.64^{+5.93}_{-4.96}$	$3.55 \pm 0.004$	$4.32 \pm 0.058$	$0.04 \pm 0.015$	$-0.76 \pm 0.027$	$7.0^{+6.42}_{-6.46}$	$7.0^{+0.75}_{-0.81}$
2M05330175-0449184	83.257301	-4.821800	$1.3^{+0.14}_{-0.20}$	$377.56^{+3.86}_{-4.44}$	$3.68 \pm 0.024$	$3.28 \pm 0.208$	...	$-0.70 \pm 0.046$	$67.0^{+66.17}_{-66.27}$	$67.0^{+4.94}_{-8.39}$
2M05330432-0519410	83.267998	-5.328100	$0.2^{+0.09}_{-0.12}$	$375.15^{+2.69}_{-2.35}$	$3.61 \pm 0.006$	$4.03 \pm 0.092$	...	$-0.27 \pm 0.020$	$3.0^{+2.29}_{-2.30}$	$3.0^{+0.14}_{-0.13}$
2M05331059-0459078	83.294098	-4.985500	$0.8^{+0.13}_{-0.15}$	$373.95^{+5.46}_{-5.00}$	$3.55 \pm 0.005$	$3.99 \pm 0.077$	$-0.04 \pm 0.019$	$-0.74 \pm 0.031$	$7.8^{+7.11}_{-7.16}$	$7.8^{+1.08}_{-0.82}$
Orion B Complex										
2M05361923-0123588	84.080101	-1.399700	$0.7^{+0.08}_{-0.05}$	$397.79^{+4.72}_{-5.06}$	$3.59 \pm 0.002$	$4.22 \pm 0.043$	$-0.09 \pm 0.006$	$-0.49 \pm 0.019$	$0.7^{+0.00}_{-0.00}$	$5.1^{+0.32}_{-0.40}$
2M05362908-0235482	84.121201	-2.596700	$0.8^{+0.05}_{-0.07}$	$359.18^{+3.40}_{-3.72}$	$3.56 \pm 0.001$	$3.98 \pm 0.029$	$0.03 \pm 0.005$	$-0.57 \pm 0.017$	$0.6^{+0.01}_{-0.01}$	$4.1^{+0.32}_{-0.30}$
2M05363302-0123334	84.137604	-1.392600	$0.5^{+0.03}_{-0.03}$	$340.99^{+1.66}_{-1.61}$	$3.64 \pm 0.001$	$4.38 \pm 0.032$	...	$0.10 \pm 0.013$	$0.8^{+0.01}_{-0.01}$	$1.4^{+0.09}_{-0.06}$
2M05363878-0254196	84.161598	-2.905500	$0.7^{+0.06}_{-0.07}$	$361.40^{+4.21}_{-4.48}$	$3.55 \pm 0.002$	$4.25 \pm 0.049$	$0.02 \pm 0.007$	$-0.71 \pm 0.018$	$0.6^{+0.01}_{-0.01}$	$6.9^{+0.59}_{-0.40}$
2M05365019-0247099	84.209198	-2.786100	$0.7^{+0.09}_{-0.08}$	$365.75^{+3.60}_{-3.79}$	$3.56 \pm 0.001$	$4.24 \pm 0.045$	$0.03 \pm 0.008$	$-0.72 \pm 0.019$	$0.7^{+0.01}_{-0.01}$	$8.4^{+0.79}_{-0.67}$
2M05365170-0210104	84.215401	-2.169600	$3.5^{+0.22}_{-0.20}$	$362.20^{+7.56}_{-9.52}$	$3.69 \pm 0.026$	$4.29 \pm 0.094$	...	$-0.17 \pm 0.062$	$1.1^{+0.03}_{-0.03}$	$12.3^{+6.54}_{-3.35}$
2M05365231-0121246	84.218002	-1.356900	$0.7^{+0.03}_{-0.03}$	$348.45^{+1.51}_{-1.95}$	$3.62 \pm 0.001$	$4.14 \pm 0.046$	...	$-0.18 \pm 0.012$	$0.7^{+0.00}_{-0.00}$	$2.4^{+0.09}_{-0.09}$
2M05365409-0253155	84.225403	-2.887700	$0.4^{+0.04}_{-0.05}$	$380.19^{+2.06}_{-2.30}$	$3.64 \pm 0.002$	$4.24 \pm 0.032$	...	$0.06 \pm 0.016$	$0.9^{+0.03}_{-0.03}$	$1.6^{+0.17}_{-0.12}$
2M05365500-0135508	84.229202	-1.597500	$0.4^{+0.03}_{-0.04}$	$419.06^{+5.39}_{-5.09}$	$3.59 \pm 0.002$	$4.26 \pm 0.053$	$-0.01 \pm 0.007$	$-0.59 \pm 0.016$	$0.7^{+0.00}_{-0.00}$	$7.6^{+0.63}_{-0.35}$
2M05365983-0120245	84.249298	-1.340100	$0.9^{+0.16}_{-0.10}$	$417.41^{+11.73}_{-9.01}$	$3.52 \pm 0.004$	$4.48 \pm 0.061$	$-0.02 \pm 0.014$	$-0.67 \pm 0.032$	$0.4^{+0.03}_{-0.03}$	$2.2^{+0.39}_{-0.32}$
Orion OB1 Complex										
2M05191549-0204529	79.814598	-2.081400	$1.6^{+0.05}_{-0.07}$	$359.50^{+8.15}_{-7.43}$	$3.55 \pm 0.002$	$4.17 \pm 0.078$	$0.01 \pm 0.009$	$-0.63 \pm 0.026$	$0.6^{+0.02}_{-0.02}$	$4.4^{+0.58}_{-0.46}$
2M05192175-0217193	79.840698	-2.288700	$0.6^{+0.02}_{-0.03}$	$349.42^{+2.09}_{-2.47}$	$3.63 \pm 0.002$	$4.44 \pm 0.036$	...	$-0.29 \pm 0.014$	$0.9^{+0.02}_{-0.02}$	$5.2^{+0.45}_{-0.38}$
2M05194349-0116397	79.931198	-1.277700	$0.4^{+0.04}_{-0.03}$	$364.45^{+3.49}_{-3.73}$	$3.58 \pm 0.001$	$4.43 \pm 0.027$	$0.02 \pm 0.006$	$-0.53 \pm 0.015$	$0.7^{+0.00}_{-0.00}$	$5.3^{+0.33}_{-0.21}$
2M05195766-0301262	79.990303	-3.024000	$0.8^{+0.02}_{-0.04}$	$351.16^{+2.00}_{-2.11}$	$3.65 \pm 0.001$	$4.50 \pm 0.025$	...	$-0.18 \pm 0.013$	$1.0^{+0.01}_{-0.01}$	$6.2^{+0.35}_{-0.28}$

**Table 4**  
(Continued)

APOGEE-ID	R.A. J2000	Decl.	$A_V$ (mag)	$r_{\text{geo}}$ (pc)	$T_{\text{eff}}$ (K)	log g	[Fe/H]	log $L/L_{\odot}$	$M/M_{\odot}$	Age (Myr)
2M05201480-0225456	80.061699	-2.429300	$0.5^{+0.05}_{-0.03}$	$335.54^{+1.47}_{-1.61}$	$3.67 \pm 0.001$	$4.43 \pm 0.034$	...	$-0.33 \pm 0.015$	$1.0^{+0.02}_{-0.01}$	$14.3^{+0.72}_{-0.95}$
2M05201885-0149010	80.078598	-1.817000	$0.8^{+0.03}_{-0.04}$	$350.42^{+2.08}_{-1.78}$	$3.65 \pm 0.002$	$4.33 \pm 0.026$	...	$-0.17 \pm 0.014$	$1.0^{+0.02}_{-0.01}$	$4.6^{+0.30}_{-0.29}$
2M05202650-0300325	80.110397	-3.009100	$1.0^{+0.07}_{-0.08}$	$339.28^{+4.65}_{-4.73}$	$3.54 \pm 0.002$	$4.31 \pm 0.078$	$0.03 \pm 0.015$	$-0.78 \pm 0.023$	$0.6^{+0.01}_{-0.01}$	$6.3^{+0.68}_{-0.55}$
2M05203382-0155237	80.140900	-1.923300	$1.0^{+0.16}_{-0.13}$	$350.53^{+3.57}_{-3.98}$	$3.57 \pm 0.007$	$4.17 \pm 0.066$	$-0.02 \pm 0.015$	$-0.52 \pm 0.030$	$0.7^{+0.05}_{-0.04}$	$4.1^{+0.41}_{-0.42}$
2M05204202-0128109	80.175102	-1.469700	$0.3^{+0.06}_{-0.06}$	$342.74^{+2.42}_{-1.91}$	$3.63 \pm 0.004$	$4.01 \pm 0.039$	...	$-0.05 \pm 0.020$	$0.7^{+0.01}_{-0.00}$	$1.6^{+0.10}_{-0.11}$
2M05205489+0102022	80.228699	1.034000	$0.4^{+0.04}_{-0.03}$	$354.09^{+1.79}_{-1.53}$	$3.65 \pm 0.003$	$4.55 \pm 0.028$	...	$-0.16 \pm 0.016$	$1.0^{+0.02}_{-0.02}$	$4.4^{+0.33}_{-0.32}$
Pleiades Cluster										
2M03465940+2431124	56.747475	24.520124	$0.1^{+0.06}_{-0.05}$	$136.89^{+0.63}_{-0.59}$	$3.99 \pm 0.006$	$3.96 \pm 0.017$	...	$1.57 \pm 0.027$	$2.3^{+0.07}_{-0.05}$	...
2M03470141+2329419	56.755917	23.494942	$0.0^{+0.00}_{-0.00}$	$134.65^{+0.32}_{-0.32}$	$3.71 \pm 0.001$	$4.65 \pm 0.011$	...	$-0.42 \pm 0.012$	$0.8^{+0.00}_{-0.00}$	$43.3^{+1.81}_{-1.60}$
2M03470358+2409349	56.764927	24.159687	$0.3^{+0.12}_{-0.10}$	$136.61^{+0.43}_{-0.37}$	$3.61 \pm 0.006$	$4.39 \pm 0.035$	...	$-1.10 \pm 0.023$	$0.6^{+0.01}_{-0.01}$	$121.8^{+6.41}_{-6.32}$
2M03470376+2336588	56.765732	23.616312	$0.6^{+0.08}_{-0.07}$	$137.70^{+0.31}_{-0.48}$	$3.57 \pm 0.002$	$4.54 \pm 0.038$	$-0.03 \pm 0.006$	$-1.06 \pm 0.018$	$0.6^{+0.01}_{-0.01}$	$43.2^{+2.73}_{-3.51}$
2M03470421+2359426	56.767555	23.995214	$0.4^{+0.04}_{-0.04}$	$134.46^{+0.45}_{-0.70}$	$3.90 \pm 0.004$	$4.05 \pm 0.023$	...	$0.92 \pm 0.018$	$1.7^{+0.02}_{-0.01}$	...
2M03470678+2342546	56.778248	23.715149	$0.2^{+0.03}_{-0.03}$	$135.60^{+0.26}_{-0.25}$	$3.70 \pm 0.002$	$4.70 \pm 0.018$	...	$-0.54 \pm 0.013$	$0.8^{+0.01}_{-0.01}$	$72.0^{+20.85}_{-16.88}$
2M03470734+2313349	56.780598	23.226358	$0.2^{+0.07}_{-0.08}$	$135.98^{+0.33}_{-0.34}$	$3.63 \pm 0.004$	$4.19 \pm 0.031$	...	$-0.91 \pm 0.017$	$0.7^{+0.01}_{-0.01}$	$118.8^{+95.79}_{-30.83}$
2M03470813+2418246	56.783913	24.306841	$0.3^{+0.08}_{-0.06}$	$134.27^{+1.11}_{-0.91}$	$3.53 \pm 0.004$	$4.69 \pm 0.045$	$0.02 \pm 0.011$	$-1.67 \pm 0.017$	$0.4^{+0.01}_{-0.01}$	...
2M03470918+2403078	56.788261	24.052174	$0.4^{+0.11}_{-0.13}$	$135.96^{+0.83}_{-0.95}$	$3.55 \pm 0.008$	$4.60 \pm 0.076$	$-0.03 \pm 0.020$	$-1.55 \pm 0.024$	$0.5^{+0.01}_{-0.01}$	$217.6^{+7.94}_{-10.05}$
2M03471352+2342515	56.806385	23.714289	$0.1^{+0.03}_{-0.03}$	$134.55^{+0.22}_{-0.29}$	$3.68 \pm 0.001$	$4.64 \pm 0.015$	...	$-0.66 \pm 0.012$	$0.8^{+0.01}_{-0.01}$	$100.8^{+25.61}_{-35.05}$
2M03471365+2349535	56.806923	23.831497	$0.0^{+0.06}_{-0.08}$	$134.42^{+0.64}_{-0.63}$	$3.53 \pm 0.003$	$4.51 \pm 0.046$	$0.01 \pm 0.014$	$-1.36 \pm 0.017$	$0.5^{+0.01}_{-0.02}$	...
Rosette Complex										
2M06322147+0450274	98.089500	4.841000	$1.6^{+0.05}_{-0.05}$	$1505.39^{+77.93}_{-70.94}$	$3.68 \pm 0.004$	$3.93 \pm 0.115$	...	$0.63 \pm 0.046$	$1.3^{+0.07}_{-0.07}$	$0.7^{+0.14}_{-0.10}$
2M06322421+0358061	98.100899	3.968400	$3.4^{+0.14}_{-0.13}$	$1632.39^{+110.22}_{-119.09}$	$3.72 \pm 0.016$	$4.34 \pm 0.091$	...	$1.03 \pm 0.070$	$2.4^{+0.25}_{-0.36}$	$0.9^{+0.33}_{-0.40}$
2M06322511+0447396	98.104698	4.794300	$1.5^{+0.04}_{-0.04}$	$1441.40^{+77.22}_{-69.04}$	$3.69 \pm 0.004$	$4.32 \pm 0.046$	...	$0.50 \pm 0.045$	$1.4^{+0.06}_{-0.06}$	$1.3^{+0.21}_{-0.22}$
2M06322658+0452383	98.110802	4.877300	$2.6^{+0.16}_{-0.13}$	$1819.46^{+655.46}_{-420.47}$	$3.64 \pm 0.015$	$3.10 \pm 0.233$	...	$0.14 \pm 0.234$	$0.8^{+0.15}_{-0.06}$	$1.1^{+1.64}_{-0.59}$
2M06322766+0445035	98.115303	4.751000	$1.3^{+0.05}_{-0.05}$	$1332.67^{+60.13}_{-58.01}$	$3.67 \pm 0.004$	$4.19 \pm 0.070$	...	$0.48 \pm 0.044$	$1.2^{+0.06}_{-0.06}$	$0.9^{+0.18}_{-0.11}$
2M06322807+0454037	98.116997	4.901000	$1.2^{+0.07}_{-0.10}$	$1409.32^{+30.00}_{-38.42}$	$3.73 \pm 0.009$	$3.66 \pm 0.251$	...	$0.92 \pm 0.035$	$2.4^{+0.07}_{-0.14}$	$1.4^{+0.30}_{-0.27}$
2M06322894+0449308	98.120598	4.825200	$1.8^{+0.17}_{-0.18}$	$1195.05^{+229.08}_{-217.10}$	$3.57 \pm 0.008$	$4.06 \pm 0.148$	$0.00 \pm 0.032$	$-0.27 \pm 0.133$	$0.5^{+0.08}_{-0.08}$	$1.3^{+1.22}_{-0.49}$
2M06322969+0501344	98.123703	5.026200	$1.5^{+0.10}_{-0.10}$	$1326.31^{+132.70}_{-108.70}$	$3.66 \pm 0.002$	$4.07 \pm 0.067$	...	$0.34 \pm 0.077$	$1.1^{+0.03}_{-0.02}$	$1.1^{+0.29}_{-0.26}$
2M06323100+0450059	98.129204	4.835000	$1.8^{+0.20}_{-0.11}$	$1371.56^{+48.69}_{-34.32}$	$3.78 \pm 0.007$	$4.15 \pm 0.072$	...	$1.15 \pm 0.042$	...	...
2M06323336+0334525	98.139000	3.581300	$1.9^{+0.18}_{-0.23}$	$1476.47^{+178.67}_{-133.81}$	$3.73 \pm 0.029$	$4.22 \pm 0.105$	...	$0.43 \pm 0.115$	$1.6^{+0.13}_{-0.13}$	$5.5^{+3.43}_{-1.92}$
Taurus Complex										
2M04331003+2433433	68.291801	24.562000	$1.1^{+0.03}_{-0.03}$	$129.97^{+0.28}_{-0.24}$	$3.62 \pm 0.001$	$3.86 \pm 0.014$	...	$-0.10 \pm 0.011$	$0.7^{+0.00}_{-0.00}$	$1.8^{+0.07}_{-0.06}$
2M04332621+2245293	68.359200	22.758200	$5.5^{+0.07}_{-0.06}$	$157.24^{+2.73}_{-2.68}$	$3.56 \pm 0.001$	$3.78 \pm 0.025$	$-0.02 \pm 0.004$	$-0.49 \pm 0.020$	$0.5^{+0.01}_{-0.01}$	$2.5^{+0.27}_{-0.31}$
2M04333278+1800436	68.386597	18.012100	$1.2^{+0.06}_{-0.05}$	$145.08^{+0.55}_{-0.46}$	$3.56 \pm 0.001$	$4.15 \pm 0.018$	$0.02 \pm 0.004$	$-0.56 \pm 0.017$	$0.6^{+0.01}_{-0.01}$	$3.4^{+0.28}_{-0.26}$
2M04333405+2421170	68.391899	24.354700	$2.2^{+0.12}_{-0.08}$	$129.32^{+0.35}_{-0.42}$	$3.59 \pm 0.001$	$3.77 \pm 0.016$	$-0.02 \pm 0.003$	$-0.02 \pm 0.016$	$0.5^{+0.01}_{-0.01}$	$0.7^{+0.04}_{-0.04}$
2M04334171+1750402	68.423798	17.844500	$1.4^{+0.08}_{-0.08}$	$143.62^{+0.63}_{-0.68}$	$3.53 \pm 0.002$	$4.29 \pm 0.031$	$-0.05 \pm 0.005$	$-0.86 \pm 0.017$	$0.5^{+0.01}_{-0.01}$	$7.5^{+0.66}_{-0.54}$
2M04334298+2235566	68.429100	22.599100	$2.1^{+0.04}_{-0.04}$	$163.29^{+3.14}_{-3.29}$	$3.54 \pm 0.001$	$4.54 \pm 0.022$	$-0.01 \pm 0.003$	$-0.67 \pm 0.020$	$0.5^{+0.01}_{-0.01}$	$3.4^{+0.32}_{-0.33}$
2M04335200+2250301	68.466698	22.841700	$1.7^{+0.06}_{-0.05}$	$160.20^{+0.47}_{-0.44}$	$3.61 \pm 0.001$	$3.65 \pm 0.013$	...	$0.08 \pm 0.012$	$0.7^{+0.01}_{-0.01}$	$0.8^{+0.04}_{-0.04}$
2M04335283+1803166	68.470100	18.054600	$1.4^{+0.10}_{-0.08}$	$144.24^{+0.67}_{-0.76}$	$3.53 \pm 0.001$	$4.32 \pm 0.022$	$-0.07 \pm 0.004$	$-0.70 \pm 0.021$	$0.4^{+0.01}_{-0.01}$	...
2M04341099+2251445	68.545799	22.862400	$2.4^{+0.06}_{-0.04}$	$160.87^{+0.57}_{-0.48}$	$3.58 \pm 0.001$	$4.05 \pm 0.018$	$0.06 \pm 0.003$	$-0.32 \pm 0.014$	$0.6^{+0.01}_{-0.01}$	$2.0^{+0.13}_{-0.11}$

**Table 4**  
(Continued)

APOGEE-ID	R.A. J2000	Decl.	$A_V$ (mag)	$r_{\text{geo}}$ (pc)	$T_{\text{eff}}$ (K)	log $g$	[Fe/H]	log $L/L_{\odot}$	$M/M_{\odot}$	Age (Myr)
2M04341527+2250309	68.563599	22.841900	$4.7^{+0.19}_{-0.11}$	$164.89^{+11.83}_{-9.73}$	$3.52 \pm 0.004$	$3.83 \pm 0.091$	...	$-1.35 \pm 0.060$	...	...
Vela C Complex										
2M08572257-4353178	134.343994	-43.888302	$1.2^{+0.11}_{-0.08}$	$801.77^{+29.63}_{-27.51}$	$3.73 \pm 0.008$	$4.02 \pm 0.144$	...	$0.06 \pm 0.040$	$1.2^{+0.04}_{-0.05}$	$13.7^{+2.77}_{-1.53}$
2M08572811-4257594	134.367203	-42.966499	$0.7^{+0.05}_{-0.05}$	$880.66^{+22.17}_{-17.35}$	$3.62 \pm 0.003$	$4.10 \pm 0.085$	...	$0.00 \pm 0.022$	$0.7^{+0.01}_{-0.01}$	$1.2^{+0.08}_{-0.06}$
2M08572851-4243479	134.368805	-42.730000	$3.5^{+0.10}_{-0.10}$	$916.20^{+54.95}_{-44.85}$	$3.72 \pm 0.012$	$3.84 \pm 0.211$	...	$0.05 \pm 0.056$	$1.2^{+0.06}_{-0.05}$	$13.4^{+2.64}_{-2.54}$
2M08573006-4323570	134.375305	-43.399200	$2.0^{+0.06}_{-0.07}$	$907.24^{+30.43}_{-23.54}$	$3.70 \pm 0.003$	$4.07 \pm 0.086$	...	$0.01 \pm 0.028$	$1.2^{+0.02}_{-0.03}$	$8.8^{+1.01}_{-0.75}$
2M08573446-4314463	134.393600	-43.246201	$0.7^{+0.07}_{-0.10}$	$899.93^{+35.97}_{-45.96}$	$3.58 \pm 0.004$	$4.45 \pm 0.092$	$0.07 \pm 0.017$	$-0.61 \pm 0.039$	$0.7^{+0.00}_{-0.00}$	$6.8^{+1.43}_{-0.82}$
2M08573501-4308355	134.395905	-43.143200	$0.9^{+0.16}_{-0.19}$	$886.26^{+43.05}_{-35.78}$	$3.60 \pm 0.006$	$4.52 \pm 0.075$	$0.03 \pm 0.019$	$-0.46 \pm 0.053$	$0.7^{+0.01}_{-0.00}$	$5.1^{+1.13}_{-0.65}$
2M08573557-4259590	134.398193	-42.999699	$1.1^{+0.16}_{-0.15}$	$849.14^{+54.82}_{-37.00}$	$3.59 \pm 0.009$	$4.11 \pm 0.114$	$-0.02 \pm 0.040$	$-0.61 \pm 0.059$	$0.7^{+0.01}_{-0.01}$	$7.6^{+1.82}_{-1.36}$
2M08573649-4310134	134.402100	-43.170399	$1.1^{+0.04}_{-0.04}$	$891.54^{+24.08}_{-21.59}$	$3.63 \pm 0.003$	$4.46 \pm 0.050$	...	$-0.10 \pm 0.024$	$0.7^{+0.01}_{-0.00}$	$2.0^{+0.20}_{-0.12}$
2M08573704-4239514	134.404404	-42.664299	$3.3^{+0.14}_{-0.15}$	$1043.98^{+155.27}_{-126.72}$	$3.59 \pm 0.008$	$4.08 \pm 0.154$	$-0.10 \pm 0.044$	$-0.12 \pm 0.090$	$0.6^{+0.06}_{-0.09}$	$1.0^{+0.51}_{-0.34}$
2M08573823-4302379	134.409302	-43.043900	$1.0^{+0.15}_{-0.16}$	$845.97^{+32.95}_{-39.12}$	$3.56 \pm 0.005$	$4.06 \pm 0.196$	$0.01 \pm 0.028$	$-0.54 \pm 0.044$	$0.6^{+0.04}_{-0.03}$	$3.2^{+0.73}_{-0.51}$
W3/W4/W5 Complex										
2M02341416+6109306	38.558998	61.158501	$1.9^{+0.26}_{-0.13}$	$2010.31^{+62.78}_{-70.57}$	$3.78 \pm 0.011$	$4.06 \pm 0.060$	...	$1.41 \pm 0.051$	$2.7^{+0.09}_{-0.08}$	$2.0^{+0.30}_{-0.30}$
2M02341820+6147375	38.575901	61.793800	$0.1^{+0.19}_{-0.28}$	$1868.00^{+84.51}_{-78.82}$	$3.70 \pm 0.022$	$4.31 \pm 0.143$	...	$0.67 \pm 0.070$	$1.8^{+0.22}_{-0.59}$	$1.2^{+0.72}_{-0.57}$
2M02342952+6147403	38.623001	61.794498	$0.0^{+0.23}_{-0.25}$	$1975.95^{+77.94}_{-73.15}$	$3.72 \pm 0.027$	$4.11 \pm 0.126$	...	$0.90 \pm 0.069$	$2.3^{+0.12}_{-0.34}$	$1.6^{+0.88}_{-0.71}$
2M02343170+6116271	38.632099	61.274200	$1.5^{+0.10}_{-0.12}$	$2040.95^{+104.60}_{-108.24}$	$3.73 \pm 0.014$	$3.84 \pm 0.201$	...	$1.01 \pm 0.053$	$2.5^{+0.11}_{-0.15}$	$1.2^{+0.41}_{-0.25}$
2M02343670+6146583	38.652901	61.782902	$1.7^{+0.12}_{-0.09}$	$1938.33^{+88.28}_{-76.38}$	$3.76 \pm 0.014$	$3.80 \pm 0.121$	...	$1.23 \pm 0.060$	$2.7^{+0.14}_{-0.16}$	$1.6^{+0.59}_{-0.41}$
2M02343995+6145231	38.666500	61.756401	$1.2^{+0.25}_{-0.18}$	$2031.93^{+56.31}_{-59.21}$	$3.74 \pm 0.022$	$3.92 \pm 0.165$	...	$1.20 \pm 0.066$	$2.8^{+0.10}_{-0.23}$	$1.2^{+0.99}_{-0.54}$
2M02345682+6142075	38.736801	61.702099	$1.9^{+0.04}_{-0.04}$	$1851.73^{+76.49}_{-72.71}$	$3.69 \pm 0.003$	$3.12 \pm 0.084$	...	$1.29 \pm 0.033$	$2.1^{+0.15}_{-0.09}$	...
2M02345825+6121161	38.742699	61.354500	$3.0^{+0.16}_{-0.23}$	$2041.91^{+164.83}_{-127.78}$	$3.73 \pm 0.022$	$4.16 \pm 0.156$	...	$1.10 \pm 0.067$	$2.6^{+0.13}_{-0.32}$	$1.1^{+0.78}_{-0.46}$
2M02350481+6110320	38.770100	61.175598	$1.9^{+0.10}_{-0.22}$	$2015.09^{+69.36}_{-87.29}$	$3.79 \pm 0.010$	$4.38 \pm 0.084$	...	$1.34 \pm 0.056$	$2.5^{+0.07}_{-0.08}$	$2.7^{+0.30}_{-0.23}$

(This table is available in its entirety in machine-readable form.)

## Appendix E

### Provisional Location for Figure Sets

This version of the manuscript contains the codes for the Figure Sets in this appendix in order to facilitate commenting and edition of the manuscript. It is expected that Figure Sets will be available for Figures 2, 4, and 5.

### ORCID iDs

Carlos G. Román-Zúñiga  <https://orcid.org/0000-0001-8600-4798>  
 Marina Kounkel  <https://orcid.org/0000-0002-5365-1267>  
 Jesús Hernández  <https://orcid.org/0000-0001-9797-5661>  
 Karla Peña Ramírez  <https://orcid.org/0000-0002-5855-401X>  
 Ricardo López-Valdivia  <https://orcid.org/0000-0002-7795-0018>  
 Kevin R. Covey  <https://orcid.org/0000-0001-6914-7797>  
 Amelia M. Stutz  <https://orcid.org/0000-0003-2300-8200>  
 Alexandre Roman-Lopes  <https://orcid.org/0000-0002-1379-4204>  
 Hunter Campbell  <https://orcid.org/0000-0001-5436-5388>  
 Elliott Khilfeh  <https://orcid.org/0000-0001-9649-6028>  
 Mauricio Tapia  <https://orcid.org/0000-0002-0506-9854>  
 Guy S. Stringfellow  <https://orcid.org/0000-0003-1479-3059>  
 Juan José Downes  <https://orcid.org/0000-0001-6559-2578>  
 Keivan G. Stassun  <https://orcid.org/0000-0002-3481-9052>  
 Dante Minniti  <https://orcid.org/0000-0002-7064-099X>  
 Amelia Bayo  <https://orcid.org/0000-0001-7868-7031>  
 Jinyoung Serena Kim  <https://orcid.org/0000-0001-6072-9344>  
 Genaro Suárez  <https://orcid.org/0000-0002-2011-4924>  
 Jason E. Ybarra  <https://orcid.org/0000-0002-3576-4508>  
 José G. Fernández-Trincado  <https://orcid.org/0000-0003-3526-5052>  
 Penélope Longa-Peña  <https://orcid.org/0000-0001-9330-5003>  
 Valeria Ramírez-Preciado  <https://orcid.org/0000-0002-4013-2716>  
 Javier Serna  <https://orcid.org/0000-0001-7351-6540>  
 Richard R. Lane  <https://orcid.org/0000-0003-1805-0316>  
 D. A. García-Hernández  <https://orcid.org/0000-0002-1693-2721>  
 Rachael L. Beaton  <https://orcid.org/0000-0002-1691-8217>  
 Dmitry Bizyaev  <https://orcid.org/0000-0002-3601-133X>  
 Kaike Pan  <https://orcid.org/0000-0002-2835-2556>

### References

Abdurro'uf, Accetta, K., Aerts, C., et al. 2022, *ApJS*, 259, 35  
 Ahumada, R., Prieto, C. A., Almeida, A., et al. 2020, *ApJS*, 249, 3  
 Anderson, G. M. 1976, *Geochim. Cosmochim. Acta*, 40, 1533  
 Astropy Collaboration, Price-Whelan, A. M., & Sipőcz, B. M. 2018, *AJ*, 156, 123  
 Astropy Collaboration, Robitaille, T. P., Tollerud, E. J., et al. 2013, *A&A*, 558, A33  
 Avedisova, V. S. 2002, *ARep*, 46, 193  
 Bailer-Jones, C. A. L., Rybizki, J., Fouesneau, M., Demleitner, M., & Andrae, R. 2021, *AJ*, 161, 147  
 Baraffé, I., Homeier, D., Allard, F., & Chabrier, G. 2015, *A&A*, 577, A42  
 Baratella, M., D'Orazi, V., Carraro, G., et al. 2020, *A&A*, 634, A34  
 Baratella, M., D'Orazi, V., Sheminova, V., et al. 2021, *A&A*, 653, A67  
 Basri, G., & Martín, E. L. 1999, *ApJ*, 510, 266  
 Beaton, R. L., Oelkers, R. J., Hayes, C. R., et al. 2021, *AJ*, 162, 302  
 Beccari, G., Petr-Gotzens, M. G., Boffin, H. M. J., et al. 2017, *A&A*, 604, A22

Bica, E., Dutra, C. M., & Barbuy, B. 2003, *A&A*, 397, 177  
 Binks, A. S., Jeffries, R. D., Jackson, R. J., et al. 2021, *MNRAS*, 505, 1280  
 Blanton, M. R., Bershady, M. A., Abolfathi, B., et al. 2017, *AJ*, 154, 28  
 Bonito, R., Prisinzano, L., Venuti, L., et al. 2020, *A&A*, 642, A56  
 Borissova, J., Roman-Lopes, A., Covey, K., et al. 2019, *AJ*, 158, 46  
 Bowen, I. S., & Vaughan, A. H. 1973, *ApOpt*, 12, 1430  
 Bravi, L., Zari, E., Sacco, G. G., et al. 2018, *A&A*, 615, A37  
 Bressan, A., Marigo, P., Girardi, L., et al. 2012, *MNRAS*, 427, 127  
 Briceño, C., Calvet, N., Hernández, J., et al. 2019, *AJ*, 157, 85  
 Caiazzo, I., Heyl, J., Richer, H., et al. 2020, *ApJL*, 901, L14  
 Cambrésy, L., Marton, G., Feher, O., Tóth, L. V., & Schneider, N. 2013, *A&A*, 557, A29  
 Campello, R. J. G. B., Moulavi, D., & Sander, J. 2013, in *Advances in Knowledge Discovery and Data Mining*, ed. J. Pei (Berlin: Springer), 160  
 Cardelli, J. A., Clayton, G. C., & Mathis, J. S. 1989, *ApJ*, 345, 245  
 Choi, J., Dotter, A., Conroy, C., et al. 2016, *ApJ*, 823, 102  
 Cottaar, M., Covey, K. R., Foster, J. B., et al. 2015, *ApJ*, 807, 27  
 Cottaar, M., Covey, K. R., Meyer, M. R., et al. 2014, *ApJ*, 794, 125  
 Cottle, J. N., Covey, K. R., Suárez, G., et al. 2018, *ApJS*, 236, 27  
 Da Rio, N., Tan, J. C., Covey, K. R., et al. 2016, *ApJ*, 818, 59  
 Da Rio, N., Tan, J. C., Covey, K. R., et al. 2017, *ApJ*, 845, 105  
 Dolan, C. J., & Mathieu, R. D. 2001, *AJ*, 121, 2124  
 Dolan, C. J., & Mathieu, R. D. 2002, *AJ*, 123, 387  
 Dotter, A. 2016, *ApJS*, 222, 8  
 Eisenstein, D. J., Weinberg, D. H., Agol, E., et al. 2011, *AJ*, 142, 72  
 Esplin, T. L., Luhman, K. L., Miller, E. B., & Mamajek, E. E. 2018, *AJ*, 156, 75  
 Fang, X.-S., Bidin, C. M., Zhao, G., Zhang, L.-Y., & Bharat Kumar, Y. 2020, *MNRAS*, 495, 2949  
 Fang, X.-S., Zhao, G., Zhao, J.-K., & Bharat Kumar, Y. 2018, *MNRAS*, 476, 908  
 Fang, X.-S., Zhao, G., Zhao, J.-K., Chen, Y.-Q., & Bharat Kumar, Y. 2016, *MNRAS*, 463, 2494  
 Fernandez, M. A., Covey, K. R., De Lee, N., et al. 2017, *PASP*, 129, 084201  
 Foster, J. B., Cottaar, M., Covey, K. R., et al. 2015, *ApJ*, 799, 136  
 Gaia Collaboration, Prusti, T., de Bruijne, J. H. J., et al. 2016, *A&A*, 595, A1  
 Galli, P. A. B., Loinard, L., Bouy, H., et al. 2019, *A&A*, 630, A137  
 García Pérez, A. E., Allende Prieto, C., Holtzman, J. A., et al. 2016, *AJ*, 151, 144  
 Gilmore, G., Randich, S., Asplund, M., et al. 2012, *Msngr*, 147, 25  
 Gossage, S., Conroy, C., Dotter, A., et al. 2018, *ApJ*, 863, 67  
 Gunn, J. E., Siegmund, W. A., Mannery, E. J., et al. 2006, *AJ*, 131, 2332  
 Hahsler, M., Piekenbrock, M., & Doran, D. 2019, *Journal of Statistical Software*, Articles, 91, 1  
 Holtzman, J. A., Shetrone, M., Johnson, J. A., et al. 2015, *AJ*, 150, 148  
 Hunt, E. L., & Reffert, S. 2021, *A&A*, 646, A104  
 Kollmeier, J. A., Zasowski, G., Rix, H.-W., et al. 2017, arXiv:1711.03234  
 Kos, J., Bland-Hawthorn, J., Buder, S., et al. 2021, *MNRAS*, 506, 4232  
 Kounkel, M., Covey, K., Suárez, G., et al. 2018, *AJ*, 156, 84  
 Lada, C. J., Lombardi, M., & Alves, J. F. 2009, *ApJ*, 703, 52  
 Lindgren, L., Hernández, J., Bombrun, A., et al. 2018, *A&A*, 616, A2  
 Luhman, K. L. 2020, *AJ*, 160, 186  
 Majewski, S. R., Schiavon, R. P., Frinchaboy, P. M., et al. 2017, *AJ*, 154, 94  
 Massi, F., Weiss, A., Elia, D., et al. 2019, *A&A*, 628, A110  
 Medina, N., Borissova, J., Kurtev, R., et al. 2021, *ApJ*, 914, 28  
 Meisner, A. M., & Finkbeiner, D. P. 2014, *ApJ*, 781, 5  
 Mejía-Narvaez, A., Bruzual, G., Sanchez, S. F., et al. 2022, *ApJS*, 261, 20  
 Nidever, D. L., Holtzman, J. A., Allende Prieto, C., et al. 2015, *AJ*, 150, 173  
 Olney, R., Kounkel, M., Schillinger, C., et al. 2020, *AJ*, 159, 182  
 Pecaut, M. J., & Mamajek, E. E. 2013, *ApJS*, 208, 9  
 Percival, S. M., Salaris, M., & Groenewegen, M. A. T. 2005, *A&A*, 429, 887  
 Porras, A., Christopher, M., Allen, L., et al. 2003, *AJ*, 126, 1916  
 R Core Team 2018, *R: A Language and Environment for Statistical Computing*, R Foundation for Statistical Computing, Vienna, Austria, <https://www.R-project.org/>  
 Ramírez-Preciado, V. G., Roman-Lopes, A., Román-Zúñiga, C. G., et al. 2020, *ApJ*, 894, 5  
 Roman-Lopes, A., Román-Zúñiga, C., Tapia, M., et al. 2018, *ApJ*, 855, 68  
 Roman-Lopes, A., Román-Zúñiga, C. G., Borissova, J., et al. 2020a, *ApJ*, 891, 107  
 Roman-Lopes, A., Román-Zúñiga, C. G., Tapia, M., Minniti, D., & Borissova, J. 2020b, *ApJS*, 247, 17  
 Santana, F. A., Beaton, R. L., Covey, K. R., et al. 2021, *AJ*, 162, 303  
 Spina, L., Randich, S., Magrini, L., et al. 2017, *A&A*, 601, A70  
 Spina, L., Randich, S., Palla, F., et al. 2014, *A&A*, 568, A2  
 Sprague, D., Culhane, C., Kounkel, M., et al. 2022, *AJ*, 163, 152

- Stutz, A. M. 2018, [MNRAS](#), 473, 4890
- Stutz, A. M., & Gould, A. 2016, [A&A](#), 590, A2
- Taylor, M. B. 2005, in ASP Conf. Ser. 347, *Astronomical Data Analysis Software and Systems XIV*, ed. P. Shopbell, M. Britton, & R. Ebert (San Francisco, CA: ASP), 29
- Ting, Y.-S., Conroy, C., Rix, H.-W., & Cargile, P. 2019, [ApJ](#), 879, 69
- Tognelli, E., Prada Moroni, P. G., & Degl'Innocenti, S. 2011, [A&A](#), 533, A109
- Wenger, M., Ochsenbein, F., Egret, D., et al. 2000, [A&AS](#), 143, 9
- Wilson, J. C., Hearty, F. R., Skrutskie, M. F., et al. 2019, [PASP](#), 131, 055001
- Wright, N. J., Jeffries, R. D., Jackson, R. J., et al. 2019, [MNRAS](#), 486, 2477
- Yao, Y., Meyer, M. R., Covey, K. R., Tan, J. C., & Da Rio, N. 2018, [ApJ](#), 869, 72
- Zasowski, G., Cohen, R. E., Chojnowski, S. D., et al. 2017, [AJ](#), 154, 198
- Zhao, G., Zhao, Y., Chu, Y., Jing, Y., & Deng, L. 2012, arXiv:1206.3569